2016

Decadal Salinity Changes in the Oceanic Subtropical Gyres and Connection to Changes in the Global Water Cycle

Bryce Andrew Melzer
University of South Carolina

Decadal Salinity Changes in the Oceanic Subtropical Gyres and Connection to Changes in the Global Water Cycle

by

Bryce Andrew Melzer

Bachelor of Science
University of South Carolina, 2015

Submitted in Partial Fulfillment of the Requirements
For the Degree of Master of Science in
Marine Science
College of Arts and Sciences
University of South Carolina
2016

Accepted by:
Subrahmanyam Bulusu, Director of Thesis
Venkat Lakshmi, Reader
Alexander Yankovsky, Reader
Cheryl L. Addy, Vice Provost and Dean of the Graduate School

ACKNOWLEDGEMENTS

This project was supported in part by the NASA Physical Oceanography Program. I would like to express my thanks to my major professor Prof. Subrahmanyam Bulusu, who has been instrumental in providing me with the skills and guidance necessary to propel me down the road to success. It was only two years ago that I outlined my professional goals to Prof. Bulusu, and since then he has worked tirelessly to ensure that I was in the best possible environment to realize these goals. I would also like to thank my committee members: Dr. Alexander Yankovsky and Prof. Venkat Lakshmi, whose positive feedback and invaluable advice greatly contributed to the following body of work. I would also like to thank the Marine Science faculty for their engaging conversations and constant encouragement, particularly Prof. George Voulgaris, who helped me get my foot in the door and aided in my development of the skills that are critical in any work environment. I would also like to thank Dr. Joseph D'Addezio for always making himself available when I was in need of personal or professional advice during my early stages. A profound appreciation goes out to my parents, who may not realize the monumental impact their moral and financial support has had on me. Lastly, I would also like to thank my companions John Howell and Torie Thomas for sticking with me all of these years.

ABSTRACT

There is evidence that the global water cycle has been undergoing an intensification over several decades as a response to increasing atmospheric temperatures, particularly in regions with skewed evaporation – precipitation (E-P) patterns such as the oceanic subtropical gyres. However, observational data (rain gauges, etc.) can be quite sparse over such areas due to the inaccessibility of open ocean regions. This study utilizes in situ data, reanalysis, and model outputs to infer interannual to decadal scale trends in surface freshwater forcing within remote, evaporation-dominated subtropical regions of the ocean as they pertain to the past and present state of the global water cycle. Emphasized in this study is the importance of utilizing a wide range of ocean parameters to strengthen and validate the inferences made from any one proxy of a given parameter.

A positive trend in sea surface salinity in the subtropical gyres revealed evidence for decadal intensification in the surface forcing of these regions. Zonal drift in the location of the salinity maximum of the south Pacific, north Atlantic, and south Indian regions implies a change in the mean near-surface currents responsible for advecting high salinity waters into the region. Additionally, a comparison of satellite, in situ, and model salinity datasets was conducted to highlight the potential applications of Aquarius and SMOS satellite-derived salinity products over oceanic regions of low observational density.

Spatial and temporal salinity trends in the five subtropical gyre regions were also analyzed over the past six decades, with a focus on the subsurface salinity of the upper 1000 m of the ocean. Our results indicate an overall salinity increase within the mixed layer, and a salinity decrease at depths greater than 200m in the global subtropical gyres over 61 years. Our analysis of decadal variability of depth-integrated mixed layer fluxes into and out of the gyres reveals little change in the strength of the mean currents through this region despite an increase in both the annual import and export of salt in the southern hemisphere gyres. This suggests that the salt content of E-P maximum waters advected into the subtropical gyres is increasing over time.

Another method of monitoring the marine branch of the global water cycle is through measurement of time variable mass over the Earth. We analyzed interannual freshwater fluxes inferred from the GRACE satellite mission and obtained striking agreement with trends observed through salinity and altimetry. The strengths of the mass concentration (mascon) processing technique relative to spherical harmonics is demonstrated. We suggest that discrepancies between sea level based and gravity based mass flux estimates are due primarily to an undersampling of the subsurface ocean, and not attributed to errors in GRACE measurement or retrieval.

TABLE OF CONTENTS

LIST OF TABLES

LIST OF FIGURES

CHAPTER 1

INTRODUCTION

Salinity in the ocean distributed based on several processes, including evaporation, precipitation, isopycnal advection, eddy diffusion, and double diffusion [*Bauer and Siedler,* 1988]. Our direct observations of salinity have historically been quite sparse, and until recently the extent to which salinity governs oceanic processes has been significantly underestimated. Remote sensing of sea surface salinity (SSS) has become one of the newest frontiers in oceanographic research, and we are now realizing just how important the role of ocean salinity can be in vertical stratification, density-driven mixing, and the global water cycle. The introduction of ESA's Soil Moisture and Ocean Salinity (SMOS) in 2009 and NASA's Aquarius satellites in 2011 have allowed us to fill in both spatial and temporal gaps in our global salinity coverage over the past few years, which was previously limited to spotty single point measurements. This study uses satellite derived salinity, Simple Ocean Data Assimilation (SODA) reanalysis and other satellite data to understand the interannual and decadal changes in Oceanic Subtropical Gyres and connection to the recent changes in the Global water cycle. The thesis is divided into five chapters:

There are five subtropical gyres in the world ocean that we study here; the North Atlantic, South Atlantic, North Pacific, South Pacific, and South Indian gyres. The oceanic subtropical gyres are regions characterized by a salinity maximum near the surface that is located near the center of the subtropical surface circulation cell. It is suggested that the global evaporation-precipitation (E-P) pattern has been intensifying as a response to a warming atmosphere, but direct measurements of such parameters over the subtropical gyres is next to none. The salinity maximum of each subtropical gyre is a result of high evaporation and little precipitation in the region, as evaporation removes freshwater from the surface ocean and precipitation adds freshwater. Consequently, salinity has often been used as a proxy for net freshwater input through the air-sea interface.

Chapter 2 examines six decades of sea surface salinity (SSS) trends about the salinity maxima of the subtropical gyres through SODA reanalysis. SSS is shown to be a strong indicator of evaporation and precipitation trends over interannual timescales, and thus is used as a diagnostic of the changing state of the oceanic branch of the global water cycle (GWC). A comparison of Aquarius and SMOS SSS with in situ and reanalysis data is conducted to determine the potential contribution that satellite observations can add to GWC studies.

Chapter 3 explores the upper ocean subsurface salinity variability from 1950-2008 using SODA. This study is complimentary to Chapter 1, as we seek to affirm that the trends present in the surface layer extend to a depth of 1000 m. Transects across the salinity maximum of each region were taken to determine the climatological vertical structure of each gyre and changes to the salinity distribution over time. Also utilized is a

salt budget of each of the subtropical gyres in order to quantify the contribution of ocean circulation variability to the observed salinity trend relative to the implied E-P trend.

Chapter 4 takes an alternative approach to inferring changes in the GWC through the use of mass variations via GRACE satellite observations of gravity anomalies. These gravity anomalies are translated into mass anomalies, which we adjust to reflect only mass anomalies due to changes in the distribution of freshwater over the surface of the earth. First we compare the recently developed mass concentration (mascon) GRACE product with a traditional spherical harmonic GRACE product to highlight the improvements in both accuracy and precision over the oceans. We then derived changes in E-P by taking the difference between total sea level anomalies (from altimetry) and the steric sea level anomalies calculated from Argo temperature and salinity profiles to estimate the sea level change due to mass gain/loss. This was used a basis to validate the interannual mass anomalies obtained from GRACE, as prior studies have been hesitant to utilize GRACE data for oceanic analysis.

Finally, Chapter 5 summarizes the findings of this body of work and states the significance and implications of this research as we look to advance our knowledge of the global water cycle and ocean salinity.

CHAPTER 2

INVESTIGATING DECADAL CHANGES IN SEA SURFACE SALINITY IN OCEANIC SUBTROPICAL GYRES[2]

[2]Melzer, B. A., and B. Subrahmanyam (2015), Investigating decadal changes in sea surface salinity in oceanic subtropical gyres, Geophys. Res. Lett., 42, doi:10.1002/ 2015GL065636.

Abstract- Sea Surface Salinity (SSS) trends over the past six decades were analyzed, as salinity can be a potential diagnostic of the acceleration pattern of the global water cycle. Global salinity data from Simple Ocean Data Assimilation (SODA) reanalysis highlight surface ocean salinity trends in evaporative-dominated subtropical gyre systems over the period of 1950-2010. Global salinity observations from NASA's Aquarius and ESA's Soil Moisture and Ocean Salinity (SMOS) missions were used with relation to more recent trends and future implications on global water cycle studies. Results indicated an average salinity increase of 0.12 psu in the subtropical gyres over the 61-year study, with the greatest increase occurring in the southern hemisphere gyres. Lateral gyre drift was also inferred through salinity, as three of five gyres showed significant drift over 60 years within their respective basins. There is evidence of periodicity related to these migrations on multi-decadal timescales. A comparison of satellite, in situ, and model simulations was conducted in an effort to resolve the near-surface salinity stratification as it pertains specifically to the subtropical gyre regions, and also to show the growing relevance of satellite data in global water cycle studies.

2.1. Introduction

Global climate change variability is a popular topic within the science community due to its potential impact on society. The primary focus of research has been on studying temperature fluctuations in the past, present, and future, in order to determine if the increase in temperature is due to anthropogenic influence as suggested by *Lean and Rind* [2009]. However, within the past decade, studies such as *Terray et al.* [2012] found a correlation within their model simulations of increased freshening in the western Pacific and salinification in the subtropical Atlantic gyres due to anthropogenic forcing.

The global water cycle is expected to have intensified as a response to anthropogenic global warming, [*Skliris et al.,* 2014; *Durack et al.,* 2012; *Helm et al.,* 2010, *Riser et al.,* 2008] since the capacity of air to hold and distribute moisture is dependent on temperature, a relationship which has been parameterized by the Clausius-Clapeyron relation [*Held and Soden*, 2006]. For this reason, the focus of many has become that of estimating freshwater fluxes over the oceans, which account for 86% of global evaporation and 78% of global precipitation [*Ren et al.,* 2014].

Direct measurement of evaporation and precipitation remain sparse over most of the ocean. Thus, the salinity distribution is frequently used as a proxy to convey areas of high or low precipitation [*Skliris et al.,* 2014; *Helm et al.,* 2010; *Lagerloef et al.,* 2010; *Hosoda et al.,* 2009; *Durack et al.,* 2012]. This long-term salinification-freshening trend has major implications for the global water cycle, particularly in areas where climatological E-P anomalies exist. Figure 2.1 shows the global sea surface salinity distribution; fresher waters (less than 35 psu) in equatorial regions and high salinity waters (greater than 36 psu) at the subtropical oceanic gyres. *Durack et al.* [2012] report

changes of +0.2 in high salinity regions (S=37), -0.2 in low salinity regions (S=33) over 5 decades. This suggests an intensification of the water cycle on the order of 2% per decade. Such intensification can potentially lead to droughts, floods, and storms of increased intensity [*Lagerloef et al.,* 2010]. The anticipation for the launch of Aquarius has caused many scientists to leave the door open for continuing the research of global freshwater flux and salt budget [*Vinogradova and Ponte,* 2013b].

2.2. Data and Methods

The ability to acquire global oceanic salinity measurements has previously been limited to numerical models and sparse observational measurements from ship tracks. In the early 2000's, Argo floats were deployed, with the ultimate goal of improving the global understanding of temperature and salinity. Additionally, with the launch of the NASA Aquarius/SAC-D mission in 2011 (mission ended on June 7, 2015), and the Soil Moisture and Ocean Salinity (SMOS) mission in 2009, salinity measurements can now be analyzed on the global scale. Here we analyze Aquarius, SMOS, Argo, and Hybrid Coordinate Ocean Model (HYCOM) and place them under inter-comparison for validation purposes of the SODA-reanalysis, and furthermore to evaluate the performance of satellite derived salinity from the Aquarius and SMOS in detecting sensitive salinity trends over long time scales, as they can potentially be valuable in climate related studies such as this.

2.2.1 HYCOM

In this study, we utilized the output from the high-resolution data assimilative Hybrid Coordinate Ocean Model (HYCOM) from 2009-2013 at 1/12° horizontal resolution [*Metzger et al.*, 2014]. HYCOM has the capability of selecting among several different vertical-mixing sub-models; this version uses K-Profile Parameterization (KPP). This feature is important for our study, as salinity distribution, especially in the surface ocean, is partly dependent on vertical mixing.

2.2.2 Aquarius and SMOS salinity

Aquarius/SAC-D, launched on June 10, 2011 and ending on June 7, 2015, was tasked to successfully make global estimations of SSS. It has a 390-km swath and covers the entire globe within 7 days. Ultimately, the mission's 1° grid spacing meets the accuracy requirement of within 0.2 psu while collecting data from global locations that have never been recorded before [*Tang et al.,* 2014]. We used Aquarius version 3.0, monthly L3 SSS data. This data set is available on a horizontal resolution of 1°x1°, and though it is coarse, this resolution is sufficient and capable of resolving the major salinity changes in the gyres over hundreds of km.

Before the Aquarius mission had begun, the SMOS mission was launched on November 2, 2009 by the European Space Agency (ESA) in partnership with the Centro para el Desarrollo Tecnologico Industrial and the Centre National d'Etudes Spatiales. The SMOS satellite has the capability of capturing surface moisture and SSS through the use of the equipped L-band 2-D interferometric radiometer. The SMOS data used for this

study is the Level 3 product, which is a monthly averaged product that is originally 1/4° grid spacing. For our study, this data was re-gridded to 1° grid spacing.

2.2.3 Argo floats data

Argo salinity profiles are assimilated into global monthly averaged data sets by the International Pacific Research Center (IPRC), University of Hawaii, which span from 2005 to 2014. Because of relatively low global float density, the IPRC uses optimal interpolation to produce a final 1°x1° gridded product for distribution. We use the surface layer IPRC product for this study. *Riser et al.* [2008] report a global salinity error 0.01 psu from recovered floats, which is sufficiently accurate for our analysis, since previous studies have suggested decadal salinity changes on the order of 0.2 psu [*Durack et al.,* 2012].

2.2.4 Simple Ocean Data Assimilation (SODA) reanalysis

The SODA reanalysis is produced from a general ocean circulation model, driven by surface forcing and corrected based on direct observations [*Carton and Giese,* 2008]. SODA v2.2.4 surface layer salinity is chosen for this study, a global product produced by the Asian Pacific Data Research Center (APDRC) at a monthly temporal resolution and a 1/2° spatial resolution, which spans from 1950-2010. Although the resolution of reanalysis data is independent of observational data, we must still keep in mind that the observational data is sparser in the early stages of the time series. Hence, any bias present in the model dynamics may be amplified back through time due to fewer direct observations with which to correct errors. Also, potential errors arise due to changes in

our global observing system, such as the introduction of satellite observations in the 1970's [*Carton and Giese, 2008*]. *Carton et al.* [2000] observed a depth-averaged RMS of less than 0.16 in the subtropics, with the largest error generally seen at and around the thermocline. Likewise, they concluded that the sources of error in SODA reanalysis salinity are primarily those associated with the mixed layer depth and subduction processes, large-scale bias, and mesoscale variability.

2.3. Results and Discussion

2.3.1 Comparison of Aquarius, SMOS, Argo, SODA, HYCOM

From the Taylor Diagram (Figure 2.2), we see that both satellites show a high correlation with Argo, and the RMSD stays below 0.2 psu in all gyres for Aquarius [*Taylor*, 2001]. This implies that the error associated with satellite data is likely sufficient for detecting salinity changes across basins on inter-annual scales. Thus, there is evidence that both Aquarius and SMOS satellites are indeed suitable to be utilized in long-term salinity studies in the subtropical gyres and climate studies.

We compared the data sets with regards to their ability to capture the SSS distribution in the subtropical gyres with low temporal deviation, with a focus on SODA since it is used in the decadal analysis. The SSS discrepancy between Argo and SODA datasets in these regions (spatially averaged boxes, see Figure 2.1) from 2005-2010 is relatively small (Figure 3 left panel). There is an overall overestimation of SODA in the oceanic subtropical regions, and an apparent underestimation in the South Pacific gyre. Also notable is the fact that the differences are lower in the Pacific basin as a whole than the differences in the Atlantic and Indian basins. The associated RMSD of <0.05 is deemed

acceptable for our purposes, although it is important to point out the aforementioned potential for model drift, which could amplify this error over time. Additional discrepancies among all data sets may be attributed in part to the variation in sampling and retrieval methods, particularly in the case of assimilated data.

Also of particular interest was the performance of the Aquarius and SMOS satellites, as their recent introduction has implications for climate related salinity studies in the near future. Near-surface salinity stratification remains a challenge when seeking accurate validation of satellite measurements using in situ observations, namely Argo arrays [*Drucker and Riser,* 2014; *Vinogradova and Ponte,* 2013a]. The CTD pump on an Argo float is generally turned off at a depth of 5m in order to keep surface film contamination out of the conductivity cell [*Riser et al.,* 2008]. The salinity gradient between the 1-2cm depth measured by satellite and the 5-10m depth of in situ samples can be significant, making satellite-derived salinity observations potentially valuable in estimating surface freshwater fluxes [*Lagerloef et al.,* 2013]. This gradient is particularly large during times of strong precipitation over the ITCZ [*Vinogradova and Ponte,* 2013a]. The magnitude of this stratification is largely dependent on the study region, which is why we chose to conduct this comparison within the subtropical gyres. *Drucker and Riser* [2014] have shown that the vertical salinity gradient in the top 7m is relatively small (+0.03 20°N-30°N, -0.07 20°S-30°S), but associated standard deviations (±0.3, ±0.27) leave a degree of uncertainty, which we would like to address with our comparison.

Figure 3 (left panel) indicates similar maxima and minima across the satellite-derived data (Aquarius and SMOS), observational data (Argo), and model simulations (HYCOM) and SODA reanalysis. The saltiest waters, above 37 psu, were

agreeably found in the North Atlantic Subtropical Gyre. Similarly, the southern subtropical gyres show a decrease in magnitude moving from the South Atlantic Subtropical Gyre (37 psu) to the South Indian Subtropical Gyre (less than 36 psu). Taking into account inherent biases in these data sets, our analysis of low RMSD error between Aquarius-Argo and SMOS-Argo for the subtropical gyres suggests that differences due to measurement depths between the satellites and Argo in these regions.

2.3.2 Salinity change in Subtropical Gyres

SODA reanalysis of 6 decades (1950-2010) of salinity changes in high-salinity subtropical gyre regions was studied (Figure 2.3 right panel). The goal was twofold: determine the SSS trend over the 61 year time, and infer the lateral gyre drift that was qualitatively observed over the same time span. We begin with the static boxes encompassing each gyre, where SSS was spatially averaged annually in each box. The box boundaries were selected in accordance with the regions of long-term positive SSS trend identified by *Durack and Wijffels* [2010], *Skliris et al.* [2014]. Each box was averaged yearly using the data from SODA (1950-2010). The rate of SSS change in each gyre was determined through a linear trend (Figure 2.3 right panel), as removal of this trend yielded high periodicity that can be linked to natural cycles (not shown). SSS increase is noted in all of these regions over the past 61 years: North Pacific (NP) 0.066 ± 0.075 psu, South Pacific (SP) 0.227 ± 0.066 psu, North Atlantic (NA) 0.030 ± 0.046 psu, South Atlantic (SA) 0.139 ± 0.046 psu, South Indian (SI) 0.127 ± 0.080 psu.

Likewise, subtropical regions outside the gyres have also increased in salinity (not shown). As we compare the subtropical gyre SSS pattern to the global subtropical SSS

pattern, an acceleration of the SSS pattern is evident in three of the five gyre regions. This was determined by taking $\Delta SSS_{BOX} - \Delta SSS_{GLOBAL}$ for each region. ΔSSS_{BOX} refers to the salinity change in each static box, and ΔSSS_{GLOBAL} is the zonally-averaged SSS change between the latitudes of ΔSSS_{BOX}. (e.g. NP ΔSSS_{BOX} is spatially averaged with bounds 160°-237°, 10°-30°N. NP ΔSSS_{GLOBAL} is then 0°-360°, 10°-30°N). With the calculation $\Delta SSS_{BOX} - \Delta SSS_{GLOBAL}$, a positive difference is representative of an accelerated SSS pattern in the gyre relative to the global. Here is the $\Delta SSS_{BOX} - \Delta SSS_{GLOBAL}$ for each subtropical gyre, in psu: NP +0.10, SP +0.04, NA +0.10, SA -0.04, SI -0.11. We see that the North Pacific and North Atlantic subtropical gyres in particular are increasing at rates that exceed the global trend (at their latitude). From these results, we conclude that although the absolute SSS change is relatively small in the Northern Pacific and Northern Atlantic gyres, the rate of change in these gyres is still large relative to the rest of the northern subtropics.

Determination of the additional factors contributing to this long-term trend is difficult, as we cannot accurately quantify horizontal and vertical advection over such large scales through surface measurements. The Southern Indian gyre has the highest range of SSS variability over the span of this analysis, likely driven by fluctuations in the Antarctic Circumpolar Current (ACC) and Indonesian Throughflow (ITF). There is a peak in SSS from the years 2001-2007, which is evident in all regions as well as the global average. This could be a response to anthropogenically forced climate change, which has been linked to changes in the hydrological cycle and convection over the oceans [*Held and Soden,* 2006]. It is also necessary to point out that this time period

coincides with the introduction of Argo, and the spike could be partially due to a substancial increase in observational data with which to correct the SODA reanalysis.

2.3.3 Decadal gyre drift from salinity

We next address the dynamic boxes, which were refined within our static boxes and capture the migration of certain gyres over time, as seen from the SSS signature. Dynamic boxes are bound to a smaller area, determined by identifying the 8°x8° box which contains the highest average SSS of the entire gyre, as illustrated in Figure 2.4. This 8°x8° size is constant, and specifically chosen because it is large enough to minimize the influence of mesoscale features in the model, but still small enough to maintain the sensitivity needed to detect the motion of the gyre center, since the magnitude of this motion is small relative to the size of the gyre. The dynamic box operates under two key assumptions in order to quantify lateral gyre drift from salinity; (a) The salinity maximum is a reasonable estimate of the center of the gyre, and (b) the movement of the central point reflects the motion of the whole gyre. Assumption (a) has been deemed an appropriate assumption based on observations of SSH, SST, and Chl-a. We see maximum (minimum) SSH, SST, and (Chl. a) occurring in the same subtropical areas where SSS is highest [*McClain et al.*, 2004]. As for the structure of salinity at the surface, it retains consistency in shape and horizontal gradient over large time scales (Figure 2.4). However, the Pacific gyres do deviate from the norm during moderate to strong El Niño Southern Oscillation (ENSO) events, as seen in the La Niña of 2010. Also, mesoscale variability contributes some spatial variability to the SODA SSS, as

previously discussed. In this manner, the size of the dynamic boxes is critical to the validity of this method, but has been verified as such.

Rates of gyre drift are calculated in each region, which is done through a linear fit of dynamic box location as a function of time (Figure 2.5). Of the five gyres analyzed from 1950-2010, three gyres showed significant (95% confidence) lateral motion over the decadal analysis. The SP Gyre has oscillated east-west over the 61 years analyzed, with a net movement of only 203 km in over six decades. There is a reversal from eastward to westward drift in 1984, which seems to coincide with a transition from cold to warm Pacific Decadal Oscillation (PDO) phase that occurs around 1980. The NA gyre has migrated eastward at an average rate of 11 ± 4 km/yr. The SI gyre has migrated westward at an average rate of 24 ± 9 km/yr. Based on the power spectral densities (not shown), there is an apparent cycle of both the SP and NA gyres at a period of 20 years, although they are out of phase. This qualitatively matches both the PDO and the Atlantic Multi-decadal Oscillation (AMO) climate oscillations. An overall increase in precipitation and decrease in upper ocean salinity during the positive PDO phase has been well documented [*Overland et al.,* 1999, *Di Lorenzo et al.,* 2009]. In addition, *Overland et al.* have also pointed out a spatial NNW/SSE salinity pattern in the North Pacific with relation to PDO. Here we provide evidence that the effects of PDO on surface salinity distribution extends as far as the subtropical south Pacific, indicating an E/W salinity pattern.

2.4. Conclusions

Average RMSD of 0.12 psu for Aquarius and 0.18 psu for SMOS, when compared to Argo, indicates that at present, salinity data from the SMOS and Aquarius satellites has the potential to compliment reanalysis models such as SODA in global water cycle studies going forward. Eastward gyre drift of 3 (11) km/yr was observed in the Subtropical South Pacific (Subtropical North Atlantic) gyres. Westward gyre drift of 24 km/yr was observed in the Subtropical South Indian gyre. Further analysis is necessary to determine the implications of this gyre movement on large-scale circulation dynamics and nutrient distribution in the upper mixed layer of these gyres on decadal timescales, as well as the influence of PDO variability on salinity in the mid-latitudes of the South Pacific.

While evidence of a pattern amplification of salinity is strong, results indicated an average salinity increase of 0.12 psu in the subtropical gyres over 61 years, which is low compared to the 50 year, +0.2 psu change seen through integrated observations and climate modeling of *Durack et al.* [2012]. Ultimately, this study helped provide evidence of SSS variability in high evaporative regions, which plays an important role in tracking freshwater fluxes over the oceans. These results have implications to global water cycle studies, suggesting an intensification of the global water cycle over the oceanic interface, which comprises most of the global freshwater inventory. An increase of salt in one region of the global ocean could also be associated with freshening of another region to maintain freshwater continuity; thus equatorial and polar regions could see related freshening trends as surface warming continues. E-P differences from the climatological mean may also exist over the continents, which would manifest as increased severity of

drought and flooding in places that have historically been susceptible to such conditions. Science communities around the globe should consider assimilating salinity into forecasting model simulations, as it has been shown to be an important factor in such processes.

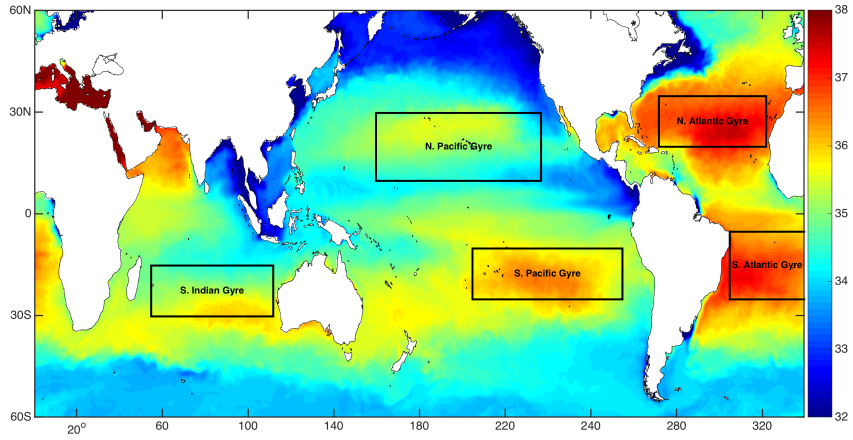

Figure 2.1: Average Sea Surface Salinity (SSS) distribution from SODA-reanalysis during 2010. The five subtropical gyre regions are defined by their respective static boxes.

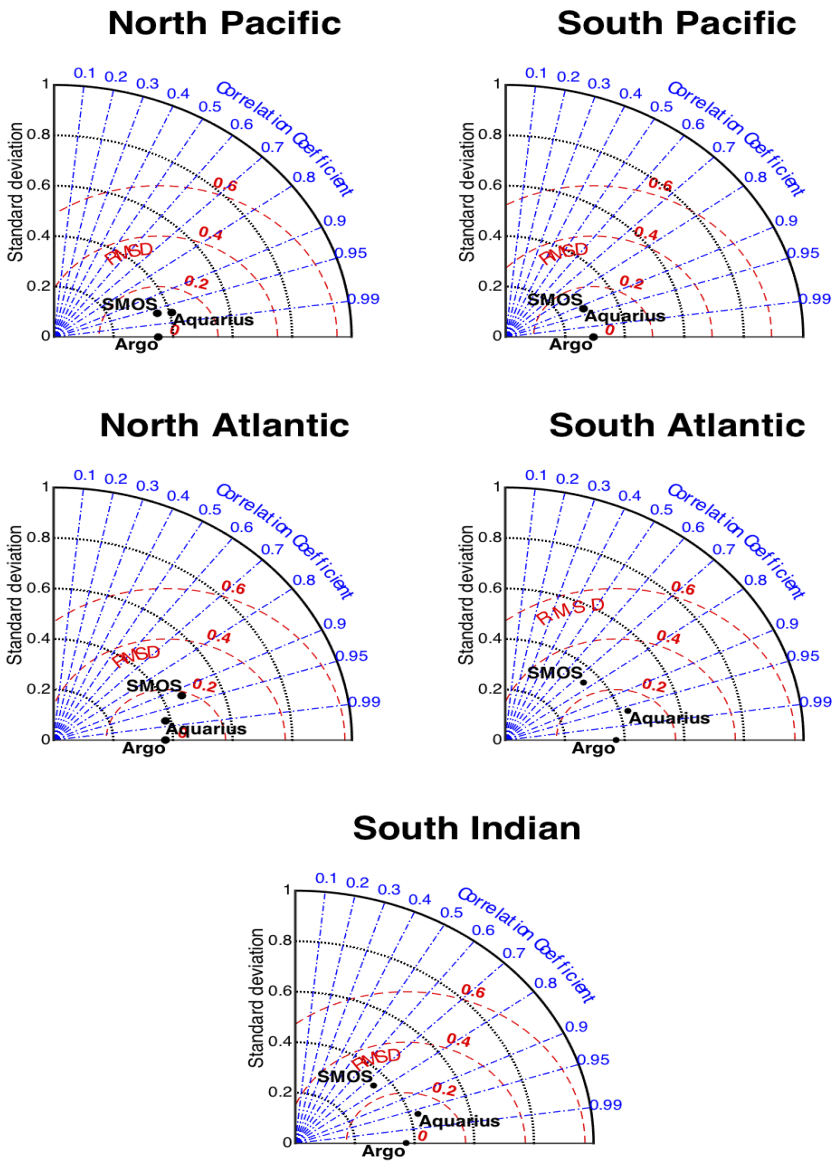

Figure 2.2: Taylor diagrams comparing Aquarius and SMOS salinity with Argo data during 2012 in the North Pacific gyre, South Pacific gyre, North Atlantic gyre, South Atlantic gyre, and South Indian gyre.

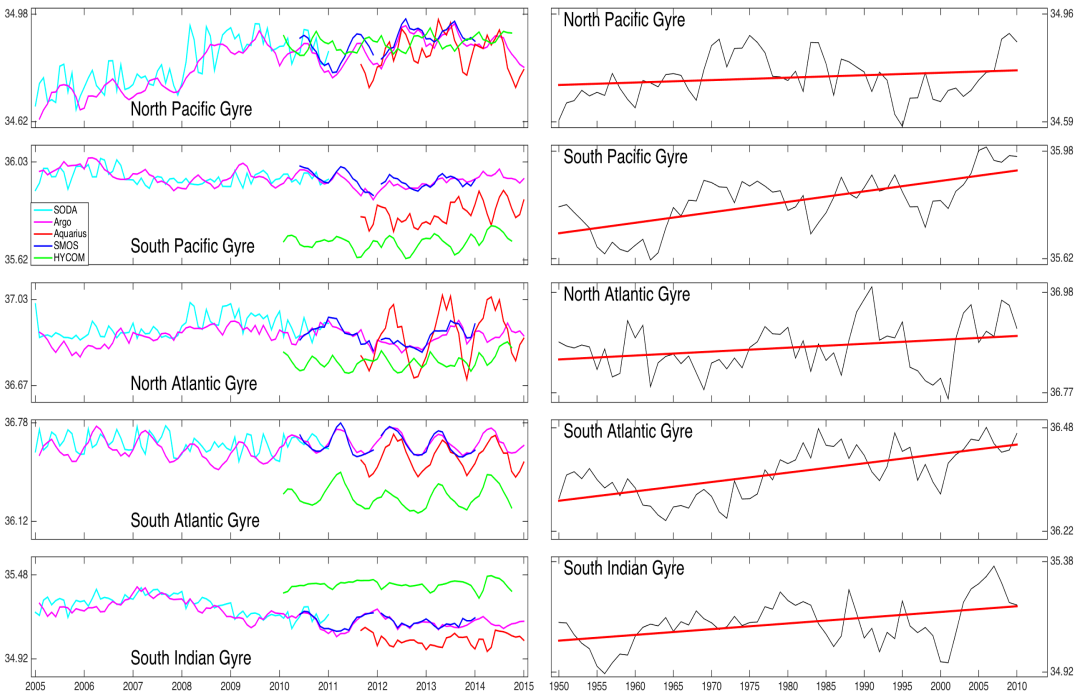

Figure 2.3: **(**left**)** 2005-2014 SSS from SODA, Argo, SMOS, Aquarius, and HYCOM data for; North Pacific gyre, South Pacific gyre, North Atlantic gyre, South Atlantic gyre, South Indian gyre. (right) corresponding gyres SSS from 1950-2013 from SODA reanalysis.

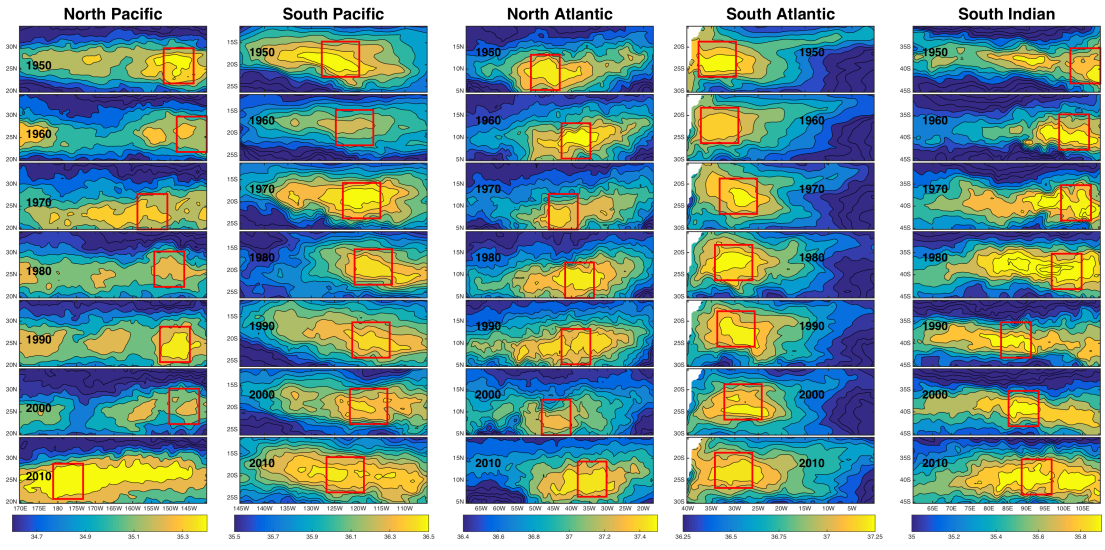

Figure 2.4: The drift of the subtropical oceanic gyres during 1950-2010. The dynamic boxes (red color) shows the drift of the high salinity maxima with a 10 year interval for North Pacific, South Pacific, North Atlantic, South Atlantic, and South Indian. Figure axes are bound by the edges of associated static boxes as shown in Figure 1.

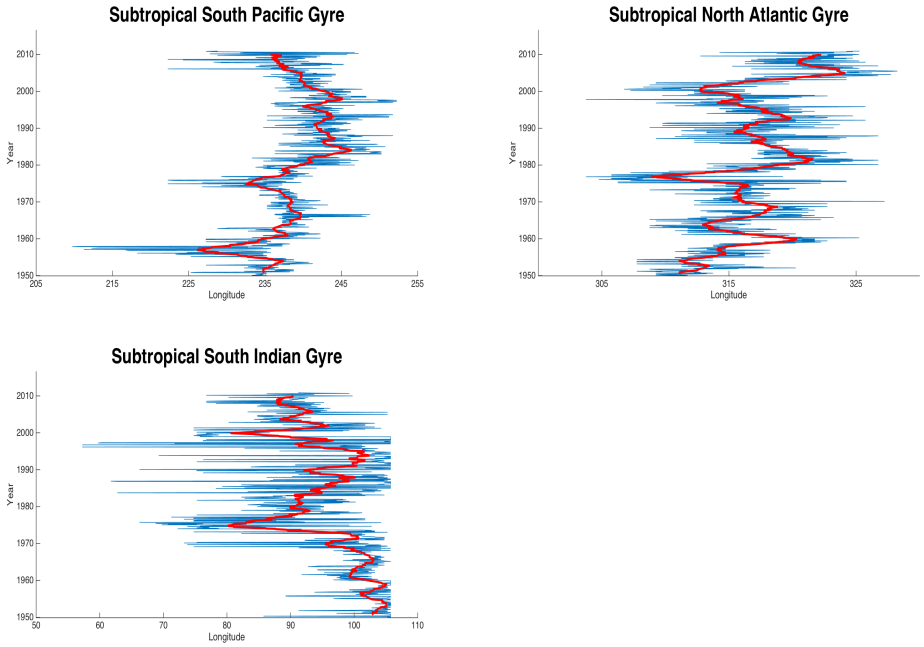

Figure 2.5: Longitude-time plot of salinity maximum in the central point of the dynamic box location for South Pacific gyre, North Atlantic gyre, and South Indian gyre. Moving-mean filter has been applied (as shown red line) to reduce noise inherent to the methodology.

CHAPTER 3

[3]DECADAL CHANGES IN SALINITY IN THE OCEANIC SUBTROPICAL GYRES

[3]Melzer, B. A., and B. Subrahmanyam. 2016. Decadal Changes in Salinity in the Oceanic Subtropical Gyres. Submitted to *Journal of Geophysical Research: Oceans*.

Abstract- We analyzed spatial and temporal salinity trends in five subtropical gyre regions over the past six decades using Simple Ocean Data Assimilation (SODA) reanalysis, with a focus on the subsurface salinity of the upper 1000 m of the ocean. Our results indicate an overall salinity increase within the mixed layer, and a salinity decrease at depths greater than 200m in the global subtropical gyres over 61 years, of which each individual gyre was analyzed in further detail. We determine that freshwater fluxes at the air-sea interface are the primary drivers of the sea surface salinity (SSS) signature over these open ocean regions by quantifying the advective contribution within the surface layer. This was demonstrated through a mixed layer salinity budget in each subtropical gyre based on the vertically integrated advection and entrainment of salt. Our analysis of decadal variability of fluxes into and out of the gyres reveals little change in the strength of the mean currents through this region despite an increase in the annual export of salt in all subtropical gyres, with the meridional component dominating the zonal. This study reveals that the salt content of E-P maximum waters advected into the subtropical gyres is increasing over time. A combination of increasing direct evaporation over the regions with increasing remote evaporation over nearby E-P maxima is believed to be the main driver in increasing salinity of the subtropical oceans, suggesting an intensification of the global water cycle over decadal timescales.

3.1. Introduction

Salinity is important with relation to the global water cycle, as changes in the collective evaporation and precipitation regimes can be reflected in the sea surface salinity (SSS) of the oceans. It is suggested that atmospheric warming will lead to increased evaporation and precipitation, as a warmer atmosphere can theoretically hold more water vapor as explained by the Clausius-Clapeyron relation [*Durack et al.,* 2012, *Held and Soden,* 2006, *Helm et al.,* 2010]. This would result in dry regions becoming increasingly dry and wet regions becoming wetter, amplifying the current spatial distribution of freshwater. The relationship between interannual salinity and freshwater forcing has already been addressed on the global scale through ECCO reanalysis [*Vinogradova and Ponte,* 2013a], which includes input from Argo, XBT, CTD, and satellite observing systems. *Yu* [2011] also showed that the mixed layer salinity is primarily driven by E-P forcing and Ekman advection over the global oceans, where E-P shows a particularly strong covariance over the subtropical gyres.

With the recent developments in satellite-derived sea surface salinity observations, we now have a better understanding of salinity processes in the surface ocean on a global scale. However, we still have limited knowledge of salinity in the subsurface, despite the established role of salinity in upper ocean stratification, freshwater fluxes, and large-scale thermohaline circulation patterns over climatological time scales. Furthermore, the subtropical gyres are generally undersampled in direct observations prior to the introduction of Argo floats to the global ocean in 2000, but there is still an ample volume of observations to drive reanalysis products such as Simple Ocean Data Assimilation (SODA), Estimating the Ocean Circulation and Climate of the Ocean (ECCO), and

Hybrid Coordinate Ocean Model (HYCOM). These regions are characterized by a strong zonal and meridional temperature gradient and basin-wide salinity maxima at the surface, which is primarily the result of high evaporation (E) and low precipitation (P) rates. Below the salinity maxima, salt is under the influence of isopycnal advection, eddy diffusion, and double diffusion (as salt fingers are prevalent in these regions) [*Bauer and Siedler,* 1988]. The variance in SSS around the salinity maxima is estimated to be explained by an even 50-50% split between surface forcing and ocean dynamics, and so we must analyze this as a coupled system [*Qu et al.,* 2011]. *Qu et al.* [2011] demonstrates this by showing that most (75%) of the salt gained directly under the E-P maximum is advected away from the source region by Ekman currents, despite the geostrophic flow in the opposite direction. The sum of E-P, advective, and diffusive forcing terms explains an estimated 75% of the variance on interannual to decadal timescales [*Dong et al.,* 2015], of which the remaining 25% is attributed to eddy mixing and entrainment. Also present are dynamic mass-conserving circulations, on the order of up to 10% of the wind driven flows, which are likewise controlled by E-P over the open ocean [*Schmitt,* 2008].

Decadal trends in salinity have already been associated with variation in evaporation and precipitation in the tropical and high latitudes [*Reul et al.,* 2013], but have only recently been analyzed thoroughly in the global subtropics [*Melzer and Subrahmanyam,* 2015]. In a study of the interannual meridional salinity of the Atlantic Ocean, *Curry et al.* [2003] found that freshwater was being lost at low latitudes and gained at high latitudes; a trend which is consistent with aforementioned studies of sea surface fluxes [*Durack et al.,* 2012]. In the subtropical North Pacific, *Lukas* [2001] has identified subsurface salinity anomalies that point to first a freshening of the upper thermocline, followed by a

salinification during the period of 1991-1997. Limitations in the temporal scale of *Lukas* has left us with further questions on the region from a climatological perspective, as the freshening was attributed to the presence of a wet (warm) Pacific Decadal Oscillation (PDO) phase, and a reversal of the trend was observed due to the major drought in the region induced by the 1997-98 El Niño. We aim to broaden the scope to all subtropical gyre regions in an effort to compare the observed trends in salinity between gyre systems and reveal how the characteristics of each gyre relates to the variable strength of the inter-gyre salinity tendency that is present, and also to quantify the relative contribution of E-P and advection to the salinity structure and salinity trend of the subtropical gyres. Here we will further analyze long-term salinity under the salinity maxima of the subtropical North Atlantic, South Atlantic, North Pacific, South Pacific, and South Indian gyres (henceforth referred to as NAG, SAG, NPG, SPG, SIG), with particular emphasis on the freshwater forcing component at the air-sea interface.

The subtropical gyres are also the gateway between low and high latitude regions, and play an important role in the transport of water masses at various levels in the ocean. The Meridional Overturning Circulation (MOC) is a key component of the heat balance of each oceanic basin, as it is responsible for poleward heat fluxes along isopycnals due to a meridional imbalance in solar heating [*Bryden et al.,* 2005]. There is now concern that a changing climate has been weakening this circulation pattern over the past few decades, with particular focus on the NAG overturning cell, as this region is responsible for the formation of NA Deep Water. Corresponding evidence for a weakening MOC has arisen from the modeling of heat fluxes over lateral transects in the subtropical Atlantic [*Zhang et al.,* 2003; *Cunningham et al.,* 2007] and Pacific [*Johnson and McPhaden*, 1999].

Changes in the MOC will be reflected in the salinity distribution, as it contributes to the high near-surface salinity and low subsurface salinity of the subtropical gyres. Construction of a mean salinity budget will aid in determining the driving component to observed changes in near-surface salinity, whether it be surface forcing, advection, or turbulent mixing.

The magnitude of meridional freshwater transfer is thought to be larger than the ability of the ocean to compensate in all subtropical gyres, particularly the NA, leaving an imbalance in freshwater flux that could be detrimental to the formation rate of North Atlantic Deep Water [*Curry et al.,* 2003]. Thus, we will derive the salt import and export from the upper ocean of the subtropical gyre regions with two objectives: First, we would like to further the findings of *Curry et al.,* [2003] by expanding analysis of freshwater balance to the Pacific and Indian basins where the dynamics controlling the salinity maxima are unique. Second, we will explore the conservative salinity forcing in the region in an attempt to explain the offset between the E-P maxima and salinity maxima in each region, and describe the remote influence of the E-P maxima on the nearby salinity maxima through advection.

3.2. Data/Methods

3.2.1. Simple Ocean Data Assimilation (SODA) Reanalysis

SODA v2.2.4 salinity and u, v, and w components of the mean (Ekman + Geostrophic) current are used for this study. These are global monthly products produced by the Asian Pacific Data Research Center (APDRC) at a 1/2° horizontal resolution, spanning from 1950-2010. The SODA reanalysis is produced from a general ocean circulation model

(POP2.x), driven by surface forcing and corrected based on direct observations. Horizontal mixing is biharmonic, while vertical mixing uses K-profile parameterization [*Carton and Giese*, 2008]. Although the resolution of reanalysis data is independent of observational data, we must still keep in mind that the observational data is sparser and may have spatial and temporal gaps in the first few decades of the time series. Hence, any bias present in the model dynamics is expected to be largest during this time due to fewer direct observations with which to correct errors, with a diminishing bias as additional observations become available for assimilation. Consequently, potential errors arise with changes in our global observing system, such as the introduction of satellite observations in the 1970s [*Carton and Giese*, 2008]. However, the introduction of the global array of Argo floats has vastly improved the number and distribution of temperature and salinity profiles in the past decade. *Carton et al.* [2000] observed a depth-averaged rmse of less than 0.16 psu in the subtropics, with the largest error generally seen at and around the thermocline. Likewise, they concluded that the sources of error in SODA reanalysis salinity are primarily those associated with the mixed layer depth and subduction processes, large-scale bias, and mesoscale variability. SODA is available at a base resolution of 40 vertical levels from 5 m to 4000 m depth, but is linearly interpolated to 2 m intervals for all mixed layer depth calculations in this study. All estimated errors associated with SODA in the results section represent standard error unless otherwise specified.

3.2.2. ECMWF Evaporation and Precipitation Reanalysis

The atmospheric climate reanalysis datasets used in this study are maintained by the European Centre for Medium-Range Weather Forecasting (ECMWF). We use the global monthly evaporation and precipitation products, which span the years 1979-2012 at a horizontal resolution of 1° × 1°.

3.2.3. Aquarius and SMOS Satellite-derived Salinity

Aquarius/SAC-D was launched on 10 June 2011 and ended on 7 June 2015. It has a 390 km swath and covers the entire globe within 7 days. Ultimately, the mission's 1° grid spacing meets the accuracy requirement of within 0.2 psu while collecting data from global locations that have never been recorded before [*Tang et al.,* 2014]. We use monthly Aquarius/SAC-D version 4.0 Level 3 mapped salinity data obtained from the Physical Oceanography Disturbed Active Archive Center (PO.DAAC).

Before the Aquarius mission had begun, the Soil Moisture and Ocean Salinity (SMOS) mission was launched on 2 November 2009 by the European Space Agency in partnership with the Centro para el Desarrollo Tecnologico Industrial and the Centre National d'Etudes Spatiales. SMOS has the capability of capturing surface moisture and SSS through the use of the equipped L band 2-D interferometric radiometer. The SMOS data used for this study is the Level 4 Centre Aval de Traitement des Données SMOS (CATDS) product obtained from the SMOS Barcelona Expert Center (BEC), a joint initiative of the Spanish Research Council (CSIC) and Technical University of Catalonia (UPC) (www.smos-bec.icm.csic.es). Almost five years of SMOS data are used from January 2010 through December 2014 on a 0.25º×0.25º grid.

3.2.4. HYCOM surface currents

In this study, we used mean surface currents in the assimilated hindcast from HYCOM (Hybrid Coordinate Ocean Model). We utilized a five-year climatology from 2009–2013 at 1/12° horizontal resolution [*Metzger et al.*, 2014]. HYCOM has the capability of selecting among several different vertical-mixing submodels; this version uses K-profile parameterization (KPP).

3.2.5. Mixed Layer Depth/Salt budget

The distribution of salinity in the subtropical gyres can also play a major role in large-scale circulation by inducing instability and oscillations in the depth of the pycnocline due to salt fingers and turbulent mixing at the base of the mixed layer [*Winton and Sarachik,* 1993]. Thus, the base of the mixed layer is important due to its role in entrainment and lateral induction of salt, driven by vertical oscillations in the mixed layer depth (MLD) and strong horizontal gradients in MLD, respectively. The thickness of the mixed layer is a function of both wind and surface buoyancy, where buoyancy is driven by heat and freshwater flux terms.

Included in our calculations of mixed layer salt balance are the horizontal advection and vertical entrainment components, leaving external surface fluxes as the final term to close the budget. While horizontal advection is primarily responsible for salt fluxes through the subtropics, entrainment across the mixed layer resulting from deepening/shoaling of the mixed layer depth has been verified as significant in high salinity regions on interannual time scales [*Qu et al.,* 2011; *Foltz and McPhaden*, 2008], and thus we will include it in our decadal analysis.

The steady state salt budget is given by the equation of mass conservation,

$$h\frac{\partial S}{\partial t} = Q_u + Q_v + S(E-P) + Q_z + \varepsilon_S \qquad (3.1)$$

where Q_u, Q_v, and Q_z are depth integrated zonal, meridional, and vertical mass transport, respectively. These terms represent horizontal advection and entrainment, while E-P gives the surface freshwater flux. They are given by the following, vertically integrated from the surface to the mixed layer depth *z*,

$$Q_u = \frac{d}{dx}\iint \rho u S \, dxdz \qquad (3.2)$$

$$Q_v = \frac{d}{dy}\iint \rho v S \, dydz \qquad (3.3)$$

$$Q_z = \frac{-W_e \Delta S}{h_m},\ W_e = \frac{\partial h_{ML}}{\partial t} \qquad (3.4)$$

where *u* and *v* are zonal and meridional velocity, *S* is the salinity, ρ is potential density, *x* and *y* are the lateral boundaries. $\frac{\partial h_{ML}}{\partial t}$ is an approximation of the entrainment/detrainment velocity [*Dong et al.,* 2015], and ΔS is the difference between the salinity at the MLD and the salinity 10 m below the base. MLD was determined to be the depth at which the density had changed by 0.125 kg/m^3 from a reference depth of 5 m, as suggested by *Monterey and Levitus* [1997]. Calculated mixed layer depths found to be greater than 80% of the total depth were determined to be invalid and discarded. ε_S (Eqn. 3.1) is the residual term, which in this case is primarily attributed to unresolved salt diffusion, assumed to be negligible for our purposes.

3.3. Results/Discussion

3.3.1. Sea surface salinity changes in the Subtropical Gyres

Our study regions (Figure 3.1) were based on the regions of long term positive SSS trend from SODA. Note that each of these regions is offset from the both the salinity max and the E-P maxima. All regions are located just south of the local salinity maximum in the poleward and westward directions because the steady state salinity maximum is generally located at the point of freshwater flux convergence as high salinity water (from E-P maximum) is pushed poleward by Ekman advection [*Dong et al.,* 2015; *O'Connor et al.*, 2005; *Rosón et al.,* 2003]. This is clearly demonstrated by the change in sign of the spatial covariance between the salinity maximum and E-P maximum, and also in the location of the boxes relative to the E-P distribution (Figure 3.2). E-P is highest along the eastern boundary of each basin, just outside the influence of the tropical rainfall bands. Because the mean location of the ITCZ is in the northern hemisphere, the salinity maxima of the southern hemisphere are consequently maintained at lower latitudes than those in the northern hemisphere, indicating the dominance of the E-P signature in the mean distribution. However, all study regions are located south of the nearby salinity maximum, which suggests advection also plays a significant role in the observed decadal SSS trends. In addition, there are dynamics specific to each region that influence the mean distribution of salinity, which we will briefly summarize.

The NPG is unique in that the box is located equatorward of the SSS max, with the northern boundary lying almost exactly on the SSS max and the southern boundary along a strong E-P gradient between the precipitation-dominated tropics and evaporation-dominated subtropics. The zonal extent of the NPG is also the same as that of the band

containing the SSS max, but the box is offset about 500 km to the east, which means it also encompasses the E-P max along the eastern boundary.

The NAG is the only region in which the SSS max is not located at the equatorward boundary of the box; it is actually in the center, indicating that in addition to being the saltiest region, the distribution of SSS is inclined to remain the same under an enhanced E-P pattern.

The Indian SSS max is fresher and located further south than its counterparts in the southern hemisphere because it receives fresher water (~34 psu) from the West Pacific warm pool which is advected through the Indonesian Throughflow, diluting the salinity of the maximum E-P region and pushing the location of the salinity maximum to the south, while the southward flowing Leeuwin current blocks fresher waters from entering via high latitudes.

The salinity maximum in the SAG is pressed up against the western boundary due to fresh water leaking into the Benguela current from the Agulhas current across the southern tip of Africa, diluting the SSS in the center of the basin [*Gordon et al.,* 2015].

As seen in Figure 3.3, high salinity water under the E-P max is carried just west of the SSS max, where it is eventually recirculated along the eastward flowing mid-latitude current of each respective basin. The NPG and SPG show relatively insignificant seasonal cycles in the mean flow, while the NAG, SAG, and SIG regions have a greater variance throughout any given year. While the two trajectories follow a similar track in the NAG, the parcel originating at the E-P max during the summer traveled 2.9 times faster than that of a winter parcel from the same initial position (0.22 m/s, 0.08 m/s). In the SAG there is actually a divergence of the trajectories as the parcels approach the

South American landmass. Parcels approaching in the fall months (Aug-Jan) are carried southwest along the coast with the Brazil current, while those approaching in the spring (Feb-Jul) are actually caught in the South Equatorial current and is carried northwest. This explains why the high salinity region wraps around the tip of Brazil in the annual mean distribution, resulting in a salinity front along the Amazon river plume due to a seasonal convergence in that region. In the SIG, the intraannual influence of documented warm-core eddies is apparent from the meandering of the trajectories and relatively small net distance traveled.

Feng et al. [2013] suggest that the intensity of the Leeuwin current has teleconnections with the ENSO cycle, and that a shift of the Pacific towards La Niña favorable conditions thus has important implications on the Leeuwin current and its influence over the Eastern Indian Ocean. The Leeuwin current carries warm, fresh water southward before wrapping around the southern tip of Australia. The region a few km west of the current, located at 30°S, 112°E, has experienced a moderate warming and freshening trend of +1°C and -0.25 psu over the length of our study (Figures 3.4, 3.5). This region is under the direct influence of warm-core eddies shed from the Leeuwin current, of which three to nine generally spawn every year, and can remain intact for up to a year [*Fang and Morrow*, 2003], making them visible even in an annual average of temperature over the region. The life and distance traveled of these eddies is proportional to the intensity of the current, while the trajectory is dependent on bottom topography. Thus, the warm and fresh anomalies we see over sixty years may be influenced by interannual changes in the overall intensity of the Leeuwin current or the seasonality of the current intensity.

In the SPG, there is a well-defined front between the warming northwest and cooling southeast halves of the region. This front is located at approximately the same longitude as the E-P max (117°W), and runs parallel to the lateral E-P gradient. However, we see no coherent pattern in the salinity trend as we do with temperature, but rather a uniform increase in salinity across the region. Thus, we attribute this temperature tendency to a change in the water mass being advected into the region rather than external surface fluxes. During the warming season, thermal low-pressure cells are present over coastal regions in the subtropics, controlling the upwelling patterns along the coastline. While the magnitude of eastern boundary upwelling diminishes with increasing latitude, it is still significant throughout the subtropics. Evidence has arisen of a greenhouse related intensification of these low-pressure cells over coastal regions, which has been observed in multiple eastern boundary regions including the Peruvian coast [*Bakun et al.,* 2010] and the California coast [*Snyder et al.,* 2003]. This increased pressure gradient implies a higher upwelling-favorable wind stress over climatological time scales. The SPG study region experiences an apparent response to an increased pressure gradient, evident in the long-term cooling trend along the eastern boundary of the SPG from 95°W to 85°W (Figure 3.4). The 60-year cooling trend is strongest during the months of September and October (not shown) during El Niño Southern Oscillation (ENSO)-neutral years, corresponding to the peak upwelling season in the Peruvian coastal system. The changes are likely driven by either an expansion of the upwelling region along the eastern boundary of the Pacific (as proposed by *Bakun* [1990] and *Vargas et al.* [2007]) or interannual changes in the low frequency baroclinic Rossby waves that propagating westward, which are likewise influenced by the wind stress curl [*Vega et al.,* 2003]. We

speculate the former, as the region that is decreasing in temperature is well within the established 3000 km zonal reach of the oxygen minimum zone associated with cold, upwelled water masses [*Fuenzalida et al.,* 2009].

When viewing the first three EOFs of the decadal salinity variability on a global scale (Figure 3.6), we see that the first seems to be the product of freshwater fluxes, as the positive trends are located in the evaporation dominated regions and the negative trends in the precipitation dominated regions. This EOF explains 38% of the yearly variance in salinity, with the second and third EOFs coming in at 22% and 19%, respectively. The spikes in the PC of the second EOF coincide with anomalies in sea ice extent. This is particularly evident in the two peaks in the time series, which correspond to the major Great Salinity Anomalies (GSA) in the Labrador Sea of '67/68 and '88/89 [*Haak et al.,* 2003]. The third EOF can be attributed to changes in upper ocean circulation patterns. Western boundary currents of the northern hemisphere are becoming warmer and fresher as observed by *Wu et al.* [2012], and again the Leeuwin current is clearly freshening in EOF3. The subtropical gyres are becoming saltier, which supports evidence of an intensified subtropical gyre circulation, as predicted by *Yu* [2007]. Together, the top three EOFs account for 90% of the total variance in multidecadal salinity anomalies.

3.3.2. Subsurface salinity variability in the subtropical gyres

3.3.2.1. Subsurface salinity profile structure

While each of the five subtropical gyres of the world ocean is relatively ubiquitous beyond 2,000 m depth, the halocline and intermediate layers are unique to each region and sensitive to change over time. Even over a large box-averaged profile (Figure 3.7),

each region has distinctive characteristics to consider before attempting to discuss mesoscale features. The NAG gyre has the highest salinity at all depths, and is also the only gyre in which the salinity gradient is always negative. The SAG gyre has both the sharpest halocline and sharpest halostad, making it fresher than the SIG gyre between 300 m and 1000 m. Contrary to the other subtropical gyres, the SIG has a salinity maximum that occurs at 150 m depth rather than the surface. All regions converge in salinity as they approach the deep ocean, composed of relatively homogenous North Atlantic Deep Water and Antarctic Bottom Water. The discrepancy between SODA and Argo salinity is most noticeable in the near-surface, as there are processes contributing to smaller scale variability that cannot be resolved in the heavily smoothed Argo gridded product.

3.3.2.2. Meridional transects

The largest increase in near-surface salinity (~0.6 psu) is seen in the SP and SI gyres; in both instances occurring between 30-37°S (Figure 3.8). In all regions, the general trend is that of a salinification in the upper 200 m, due to increased net evaporation and advection of water masses with a comparable trend in salinity, and a freshening at depths greater than 200 m, likely forced by increased rainfall at higher latitudes and southward advection from the prevailing westerlies [*Durack,* 2015]. There also exists a meridional pattern in the trend, as the region of increasing salinity spreads deeper at low latitudes than at the mid-latitudes, with this slope closely following the 26 kg m^{-3} isopycnal, again suggesting the influx of a distinctly fresher water mass recirculated from the western boundary current of each basin.

The exception to the depth-latitude relationship is the NAG, which has a lateral

structure and depth structure independent of one another. As mentioned prior for the southern hemisphere, we again see in the NAG that the increase in salinity is concentrated at 30-37° latitude, penetrating the entire 900 m depth range of the transect. South of 30°N, the trend slowly shifts to a freshening pattern at all depths over several thousand km. At 37°N there is a strong front in which the trend shifts from +0.26 psu to -0.21 psu over a distance of only 60 km, marking the location of diverging water masses just southwest of the Azores in the NAG. The narrow width of this band that separates the freshening north of 38°N and salinification south of 37°N shows that there is very little interannual meandering between subtropical and subpolar water masses, contrary to the large intraannual variability due to the formation of mesoscale eddies [*Tychensky et al.,* 1998]. The vertical extension of 800 m is double that observed by *Gould* [1985], and displaced approximately 150 km north of the location analyzed by *Rudnick* [1996]. The gradient persists throughout the zonally averaged transect of the gyre as well, perhaps marking the Azores front as an important feature in long term studies of the meridional overturning circulation of the NAG.

3.3.2.3. Zonal transects

First, the mean salinity distribution is noted in each gyre along zonal transects, where the center of each gyre is denoted by a salinity maximum at the surface and a strong lateral gradient along the eastern boundary (Figure 3.9). The subtropical SIG gyre, however, has a salinity maximum that occurs around 100 m depth. This feature has been documented by *Stramma* [1992], and is produced by two distinct water masses. The warm, fresh, tropical surface water is carried south from the region of excess

precipitation and lays on top of the colder, saltier surface waters carried north from the region of low precipitation at 32°S. Also of significance is the duality of salinity maxima that exists in all five subtropical gyres. Each subtropical gyre has two separate local salinity maxima that are spaced approximately 90-550 km apart, separated by a "fresh tongue" region where salinity is ~0.2 psu lower. These tongues have shallower isohalines and deeper isothermals to a depth of 200 m, consistent with a downward displacement of isopycnals and subsequent detrainment due to Ekman convergence at the surface. There also appears to be a relationship linking both the zonal symmetry of the salinity distribution and the extent of the central "fresh tongue" with the bathymetry of the region. In regions where the bathymetry is ubiquitous such as the SA subtropical gyre, the salinity distribution is laterally symmetric across the fresh tongue regions. In regions with major ridge systems located within 400km of the center of circulation (i.e. SP, NA), the salinity maximum on the ridge side is 0.1 psu higher and slightly larger in volume than its counterpart. This could be due to increased vertical mixing resultant from the semi-diurnal internal tide that is generated through interaction with major ocean ridge systems [*Garrett and Kunze,* 2007]. Additionally, recirculated Subtropical Mode Water can be easily distinguished by the salinity maximum at 100-300 m depth in the region between 65°W and 55°W in a lateral transect of climatological salinity [*Curry et al.,* 2003].

Shifting to transects of mean salinity along the positive ΔSSS regions (Figure 3.10), we see a much different structure. All transects across the positive ΔSSS regions are located south of the SSS max region. Additionally, the local max along these transects is located further west in every region, with the SIG being the exception with box local

maxima to the east of the 90°E basin SSS maximum. There is now a subsurface salinity maximum in both Pacific sections, a feature not present in along the SSS max transect. They are located at 100 m depth in the NP and 150 m in the SPG, important with regards to entrainment values in these regions due to the positive salinity gradient at the base of the mixed layer.

Shifting to the decadal salt tendency along the Figure 3.11 transects, we generally see the positive trend which was prevalent at the surface in our meridional transects. The SPG shows the strongest trend in the upper 200 m of all study regions (up to 0.11 psu/decade). Across all regions, the trend is of greater intensity on the eastern boundary of the gyre. Variance in the vertical extent of the positive trend closely follows isopycnals, as is expected in a stable water column. This is particularly evident in the SPG, where the salinification extends deeper in the west, closely following the slope of the 26 kg m^{-3} density line, but also consistent in the SIG and SAG. The positive SSS trend is robust to a depth of 200-250 m. The decadal trend follows the mean salt distribution in the NPG and SAG regions, while there does not seem to be a coherent pattern in the other regions.

3.3.3. Mixed Layer Salt Budget

All subtropical gyre regions have a net poleward salt flux, but there is variability in the strength of this transport (Figure 3.12). The highest meridional salt transport is in the NPG, while the lowest is in the SIG. There is a higher meridional salt flux along the equatorward boundary of each respective box, as our boxes are offset towards lower latitudes to focus on the E-P maximum region. Likewise, the zonal transport is highest in

the NP because it incorporates the North Equatorial Current from 15°N to 20°N, which is very strong relative to the rest of the subtropical open ocean. The net zonal transport is to the east along the poleward boundary of our boxes and to the west in the southern boundary, reflective of the surface circulation pattern around the center of each subtropical gyre.

Any imbalance in the net salinity transport (Table 3.1) is assumed to be due to the addition or loss of freshwater at the surface of the ocean due to the mean E-P pattern, as entrainment was found to be negligible on the decadal level. A relatively balanced salinity transfer is observed in both Pacific basins, while the Atlantic and Indian basins have a net import. This reinforces the fact that the Atlantic and Indian subtropics are higher in climatological salinity than the Pacific. The highest rate contained in the SIG region (7.66×10^7 kg s^{-1}), despite the NAG being the saltiest study region. This is because the vertical transport of salt is much higher in the Indian region, as seen in the subsurface salinity maximum due to the lack of a well-developed pycnocline resulting from the interaction of the anomalously positive salinity gradient with the expected negative temperature gradient. This salinity maximum lies below the mixed layer confines of our budget and thus contributes to the anomalous salinity values in this area.

Despite the climatological convergence of salt in the Atlantic and Indian regions, the balance of salinity in these regions is also trending towards higher export over time (Table 3.1), of which the meridional component of the mean current is dominant in inducing the observed changes, particularly in the NPG. This is a result of a higher increase in outward transport developing along the poleward boundary and a lower increase in incoming transport along the equatorward boundary, consistent in every study

region (not shown). When decomposing this trend, we notice that the mean currents remain relatively constant over the time series, while the salinity of the water advected is the main contributor to observed changes in mass transport. The net poleward meridional salt transport in the SPG and SAG regions has strengthened by an average of 19% ± 11%, while the poleward transport has weakened in the NPG and NAG regions by an average of 4.5% ± 6%. The strongest decrease is found in the NAG, which supports previous studies of the MOC that have suggested a weakening of the circulation based on observations of increased southward motion of mixed layer and thermocline water masses in the middle of the basin [*Bryden et al.,* 2005; *Timmerman and Goosse*, 2004]. The same trend is true for zonal transport, which implies that in the northern hemisphere, less salt is being carried to the northeast, while in the southern hemisphere more salt is being carried to the southwest.

The changes in salt transport are fairly proportional with regards to the climatological mean transport over the regions (i.e. large magnitude of transport tends to fluctuate by a larger magnitude). We conclude that changes in ocean circulation are working to compensate for an increase in E-P of the subtropical gyres, but are not exporting enough salt to balance the budget over longer time scales. The largest trend in decadal salt import is present in the NPG (0.58×10^6 kg s^{-1}), where the change in SSS is very low. This suggests that even with no change in SSS, it is likely that E-P in the NPG is in fact increasing, but is being counteracted by the advective component of the salinity budget.

3.3.4. Box-Averaged trends

Taking the box average of salinity over the 1950-2008 span, we see that even on scales of thousands of square kilometers there is a positive trend in all regions, consistent with trends found at the skin layer [*Durack et al.,* 2012; *Melzer and Subrahmanyam*, 2015], but diminishing in magnitude with depth. The change in SSS in nearly six decades ranges from +0.1 ± 0.07 psu in the NPG to +0.4 ± 0.08 psu in the SIG (Figure 3.13). In conjunction with the observations of *Durack and Wijffels* [2010], SODA indicates that the region of increasing salinity reaches closer to the poles than previously thought, extending as far as 30°N and 45°S. We should point out that the salinity of all subtropical gyres increases at an anomalously high rate between the years of 2001 and 2008, with the most pronounced spikes occurring in the historically under sampled regions. This corresponds to the addition of Argo floats to the observational array for salinity, and may be an indication of inherent uncertainties in SODA salinity prior to the Argo era [*Balmaseda et al.,* 2007]. Because of this, it is difficult to validate these results due to the spottiness of data in the southern hemisphere, although we do acknowledge that ECCO-2 (Estimating the Circulation and Climate of the Ocean, Phase II) reanalysis also shows a trend of similar amplitude over the most recent couple of decades (not shown).

Around 600 m depth, the SA gyre experiences a negative temperature (not shown) and salinity trend. This is the same transitional depth at which the vertical temperature and salinity gradients change sign, indicating that regions above the base of the pycnocline are getting warmer and saltier, while the underlying layer of perennial Subtropical Mode Water is getting colder and fresher. These trends present counteracting forces on the density of the water mass. The upper layer is decreasing in density while the underlying

layer is increasing, pointing to an increased vertical stratification of the water column over the duration of the study.

3.4. Conclusions

With the recent addition of satellite-derived salinity observations, a new emphasis on ocean salinity has revealed that salinity plays a larger role in upper ocean processes than previously thought. As evidence of an accelerated global water cycle continues to emerge, we look to salinity as one means of monitoring the oceanic branch of the water cycle by using it as a proxy for evaporation minus precipitation. Here we have provided insight as to the geographical location of the subtropical regions of positive decadal salinity trend by analyzing the advective pathways that connect the E-P maximum to the salinity maximum in each individual region. Despite the increase in salt export of all study regions, there still persists a positive trend in near surface salinity of all five subtropical study regions. When comparing SSS trends to atmospheric reanalysis, it becomes apparent that the increasing salinity of the subtropical gyres is a response to an increasing rate of evaporation over several decades, with relatively small change in Ekman and geostrophic advection. Thus, we conclude that the observed increase in upper ocean salinity is primarily attributed to changes in non-conservative surface forcing rather than conservative advective or diffusive processes. Such an acceleration in the global water cycle could potentially lead to storms of increased severity, as well as intense drought and flooding events [*Terray et al.,* 2012; *Trenberth,* 2011]. Higher concentrations of water vapor in the atmosphere may also provide a positive feedback to global warming, as water vapor is a potent greenhouse gas.

Nevertheless, we must be very conservative with our conclusions due to the large uncertainties of reanalysis products, particularly in the southern hemisphere, which has been plagued with sparse observations until recent decades. Some of the regional trends identified in this study may be suitable targets for in-depth observational analyses, as SODA reanalysis is capable of identifying trends but often leaves us speculating as to how these apparent climate fluctuations affect the local and mesoscale dynamics of a given region. Pertaining to SSS as a proxy for E-P, the recent launch of the Soil Moisture Active Passive (SMAP) satellite by NASA in 2015 will be instrumental in improving our understanding of synoptic and mesoscale salinity processes by providing observations with a global coverage every 8 days at an unprecedented spatial resolution of 40 km to compliment the ever-growing array of Argo floats in the global ocean.

Table 3.1: (Q_{in}) climatological average salt transport *into* each of the boxed regions from Figure 1. (ΔQ_{in}) 1950-2008 linear change in Q_{in}. Also given are the relative contributions of the zonal and meridional mean current components to the observed change in salt transport into the study regions.

Subtropical Gyre Region	**(Q_{in}) [10^6 kg s^{-1}]**	**ΔQ_{in} [10^6 kg s^{-1}/59 yr]**	**ΔQ_{in} Zonal**	**ΔQ_{in} Meridional**
North Pacific (NPG)	-2.6	-0.58	15%	85%
South Pacific (SPG)	-1.3	-0.10	34%	66%
North Atlantic (NAG)	8.5	-0.12	34%	66%
South Atlantic (SAG)	16.8	-0.02	28%	72%
South Indian (SIG)	76.6	-0.01	48%	52%

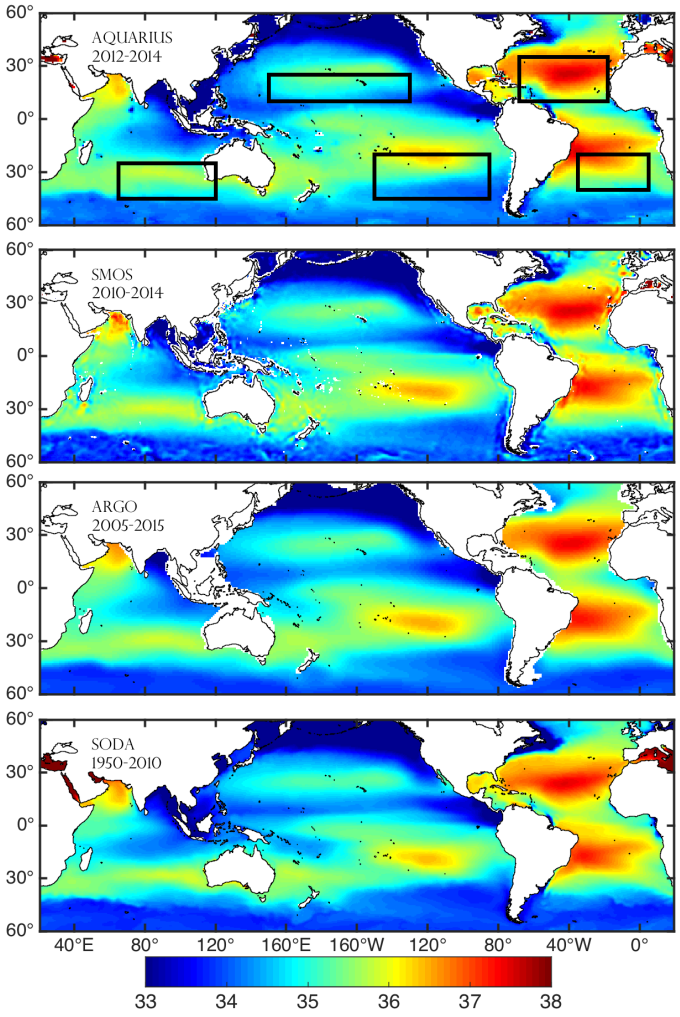

Figure 3.1: Climatological sea surface salinity [psu] over the global ocean for each of the indicated data sources, with boxes denoting the subtropical gyre study regions of each basin.

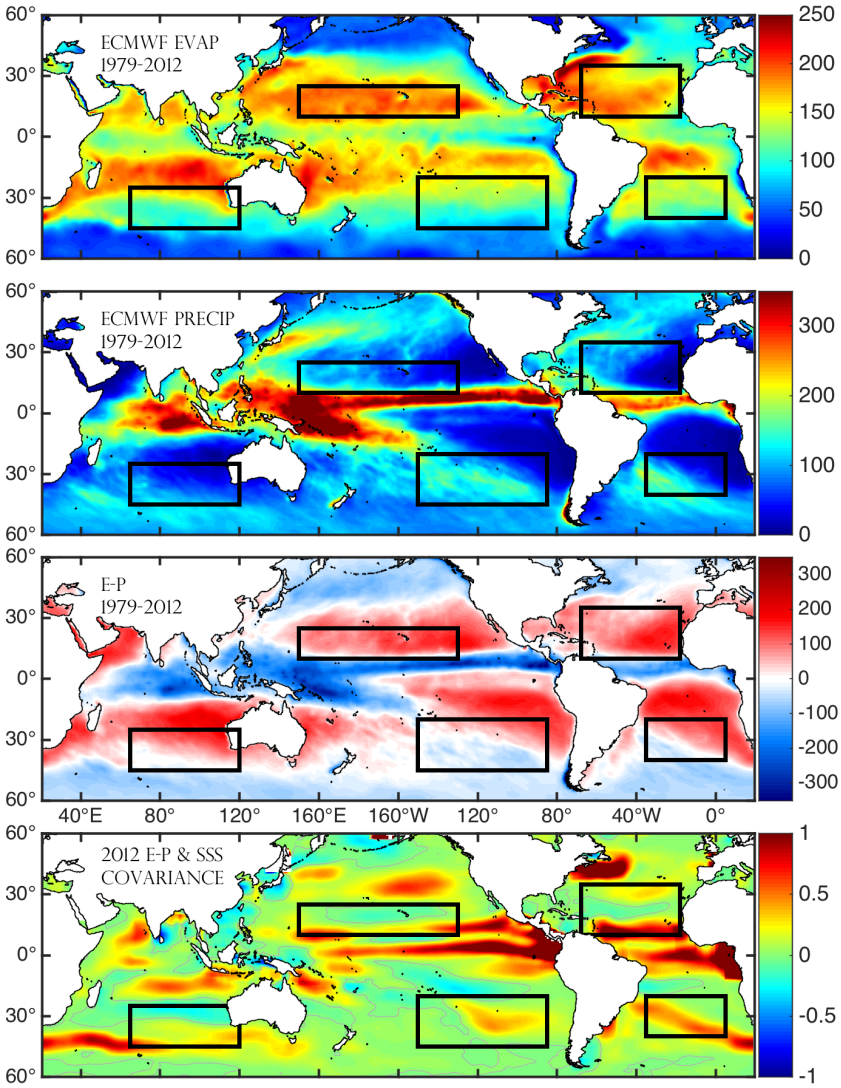

Figure 3.2: Climatological (a) evaporation [E], (b) precipitation [P], (c) E-P, and (d) Normalized spatial covariance between E-P and SSS, with boxes denoting the subtropical gyre study regions of each basin [cm/yr].

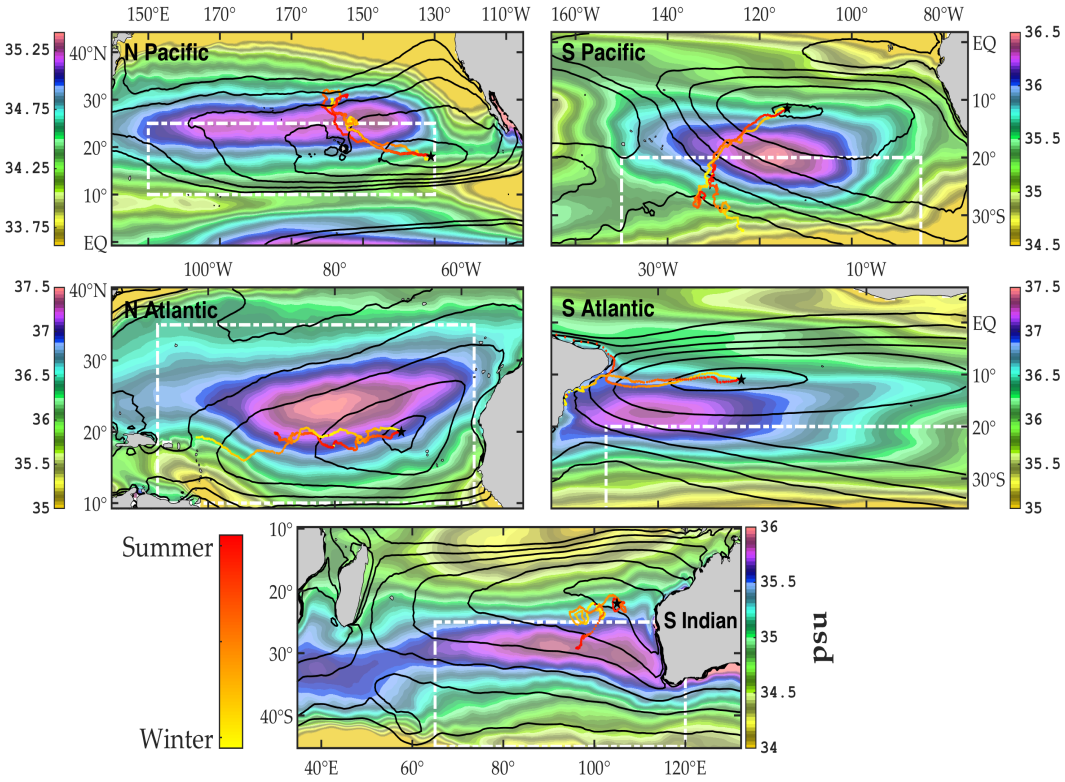

Figure 3.3: Climatological SSS (shading) and E-P (contour) in each of the indicated subtropical gyre regions from SODA and ECMWF, respectively. Boxes (white) reference regions of positive SSS trend. Stars indicate the maximum E-P of each region, and the two lines (red/yellow) are 365-day particle trajectories with a time step of 1 day using climatological HYCOM surface currents. One trajectory is initiated on January 1 and one is initiated on July 1, with shading indicative of the time elapsed at each step.

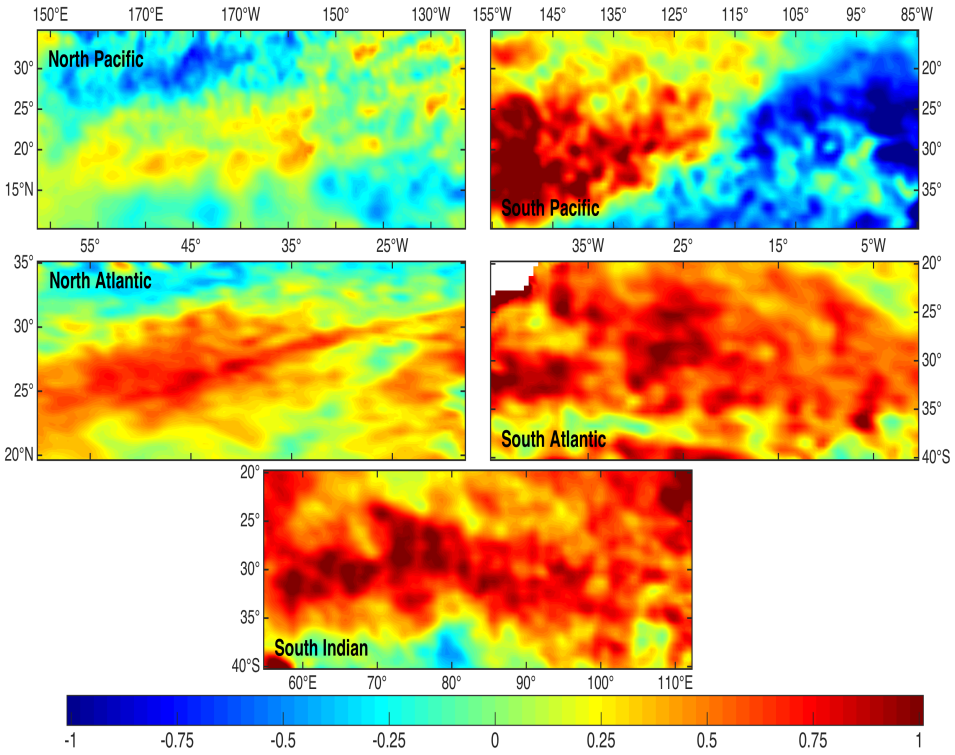

Figure 3.4: 1950-2008 temperature change (linear) at 5 m depth in the regions specified in Figure 1 from SODA [°C].

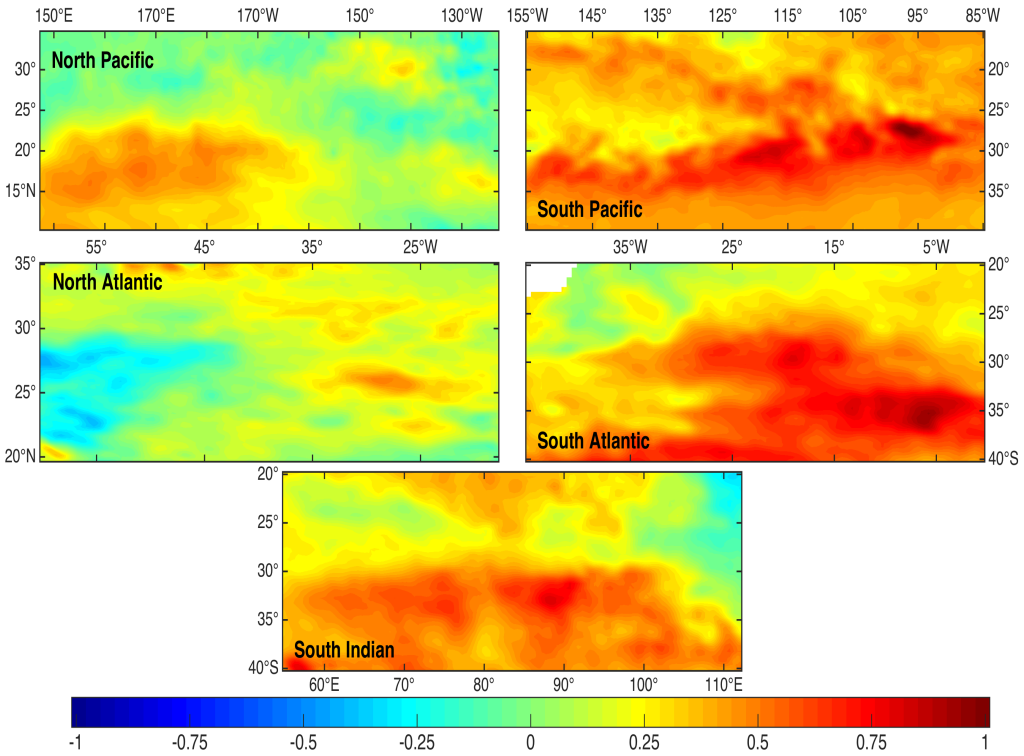

Figure 3.5: 1950-2008 salinity change (linear) at 5 m depth in the regions specified in Figure 1 from SODA [psu].

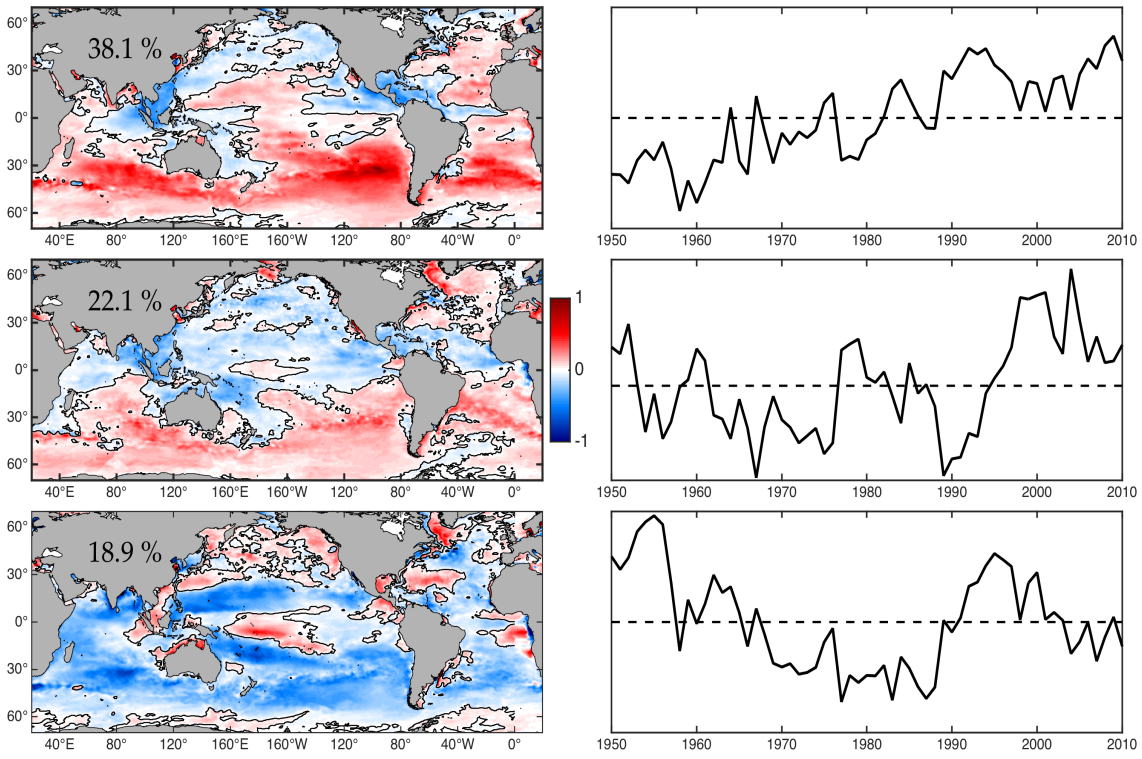

Figure 3.6: EOFs and PCs 1-3 of yearly (1950-2010) SSS fields from SODA and their temporal variability. Each map has been normalized, with the percent variance given in the top left.

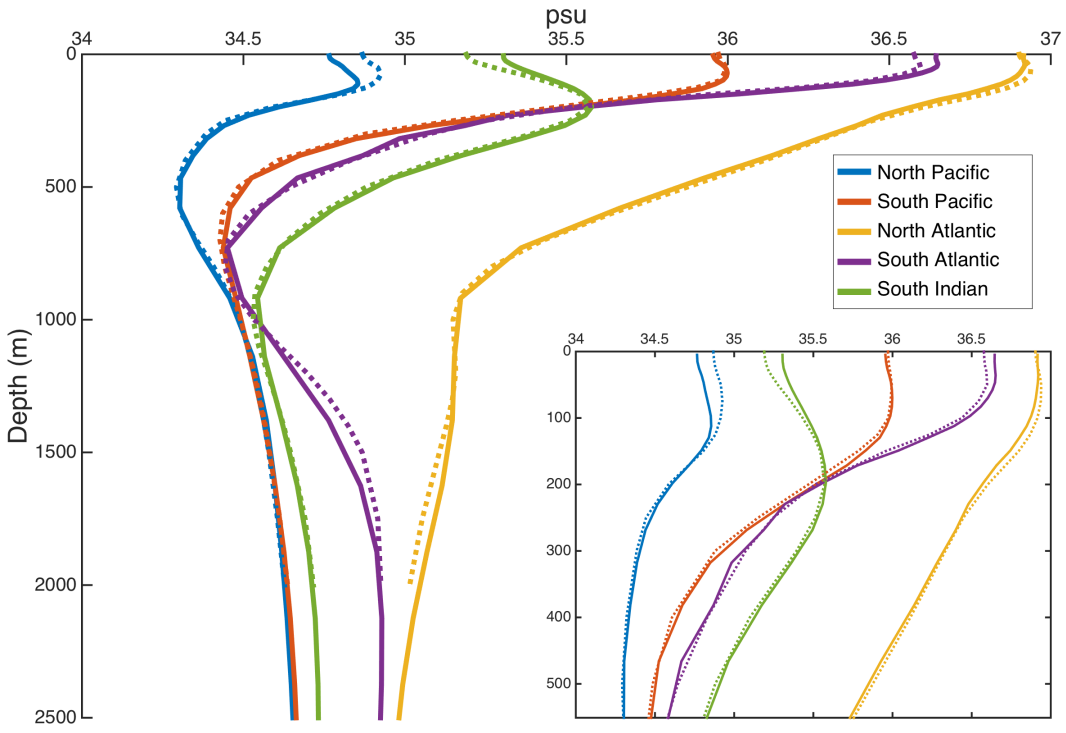

Figure 3.7: Spatially averaged annual sea surface salinity (psu) profiles to a) 4000m and b) 500m during 2010 from SODA (solid) and Argo (dotted) in a) North Pacific gyre (NPG), b) South Pacific gyre (SPG), c) North Atlantic gyre (NAG), d) South Atlantic gyre (SAG), e) South Indian gyre (SIG) after removal of seasonal variability.

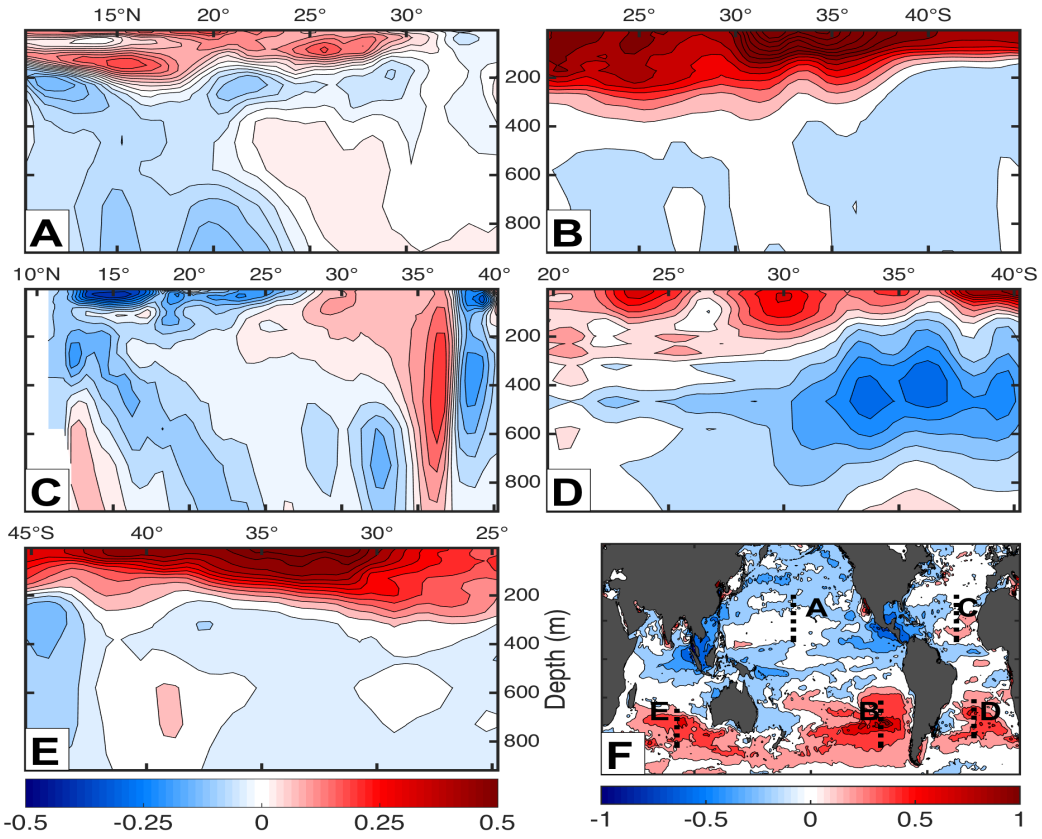

Figure 3.8: (a-e) Latitude-depth transects of 1950-2008 linear salinity trend from SODA to a maximum of 900 m depth [psu]. The colorbar south of (e) applies to panels (a)-(e). (f) Map of multidecadal linear SSS trend [psu] from 60°N-60°S. Dotted lines indicate profile sections taken in (a)-(e), corresponding to positive SSS trend from SODA.

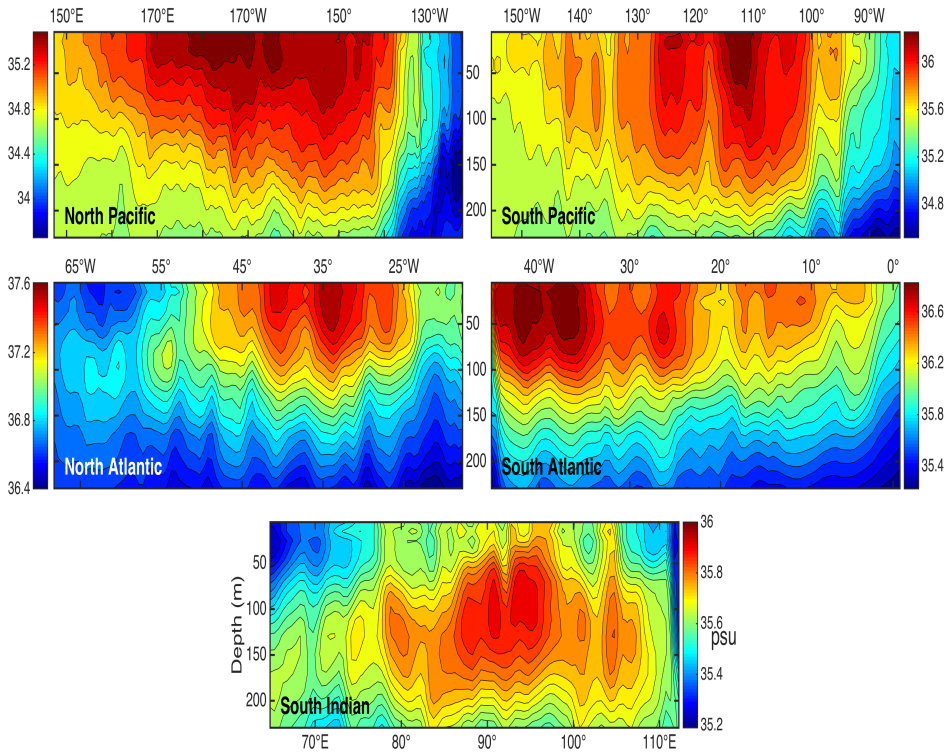

Figure 3.9: Longitude-depth plot of SODA 1950-2010 climatological mean salinity [psu] along the 25°N/S transects of each subtropical gyre from SODA, corresponding to the SSS max region of each gyre.

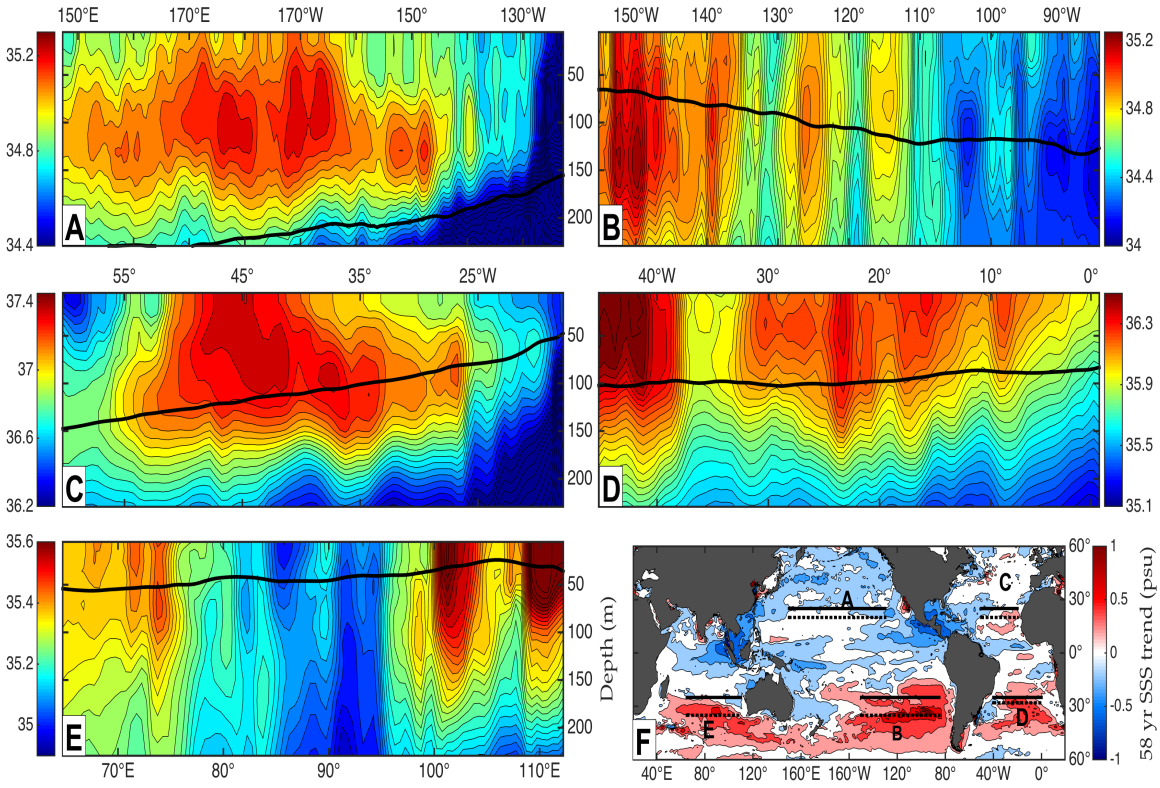

Figure 3.10: (a-e) Longitude-depth transects of 1950-2008 climatological mean salinity from SODA to a maximum of 900 m depth [psu]. Black contour marks the 26 kg m^{-3} line of constant density. (f) Map of multidecadal linear SSS trend [psu] from 60°N-60°S. Dotted lines indicate profile sections taken in (a)-(e), corresponding to regions of positive SSS trend from SODA.

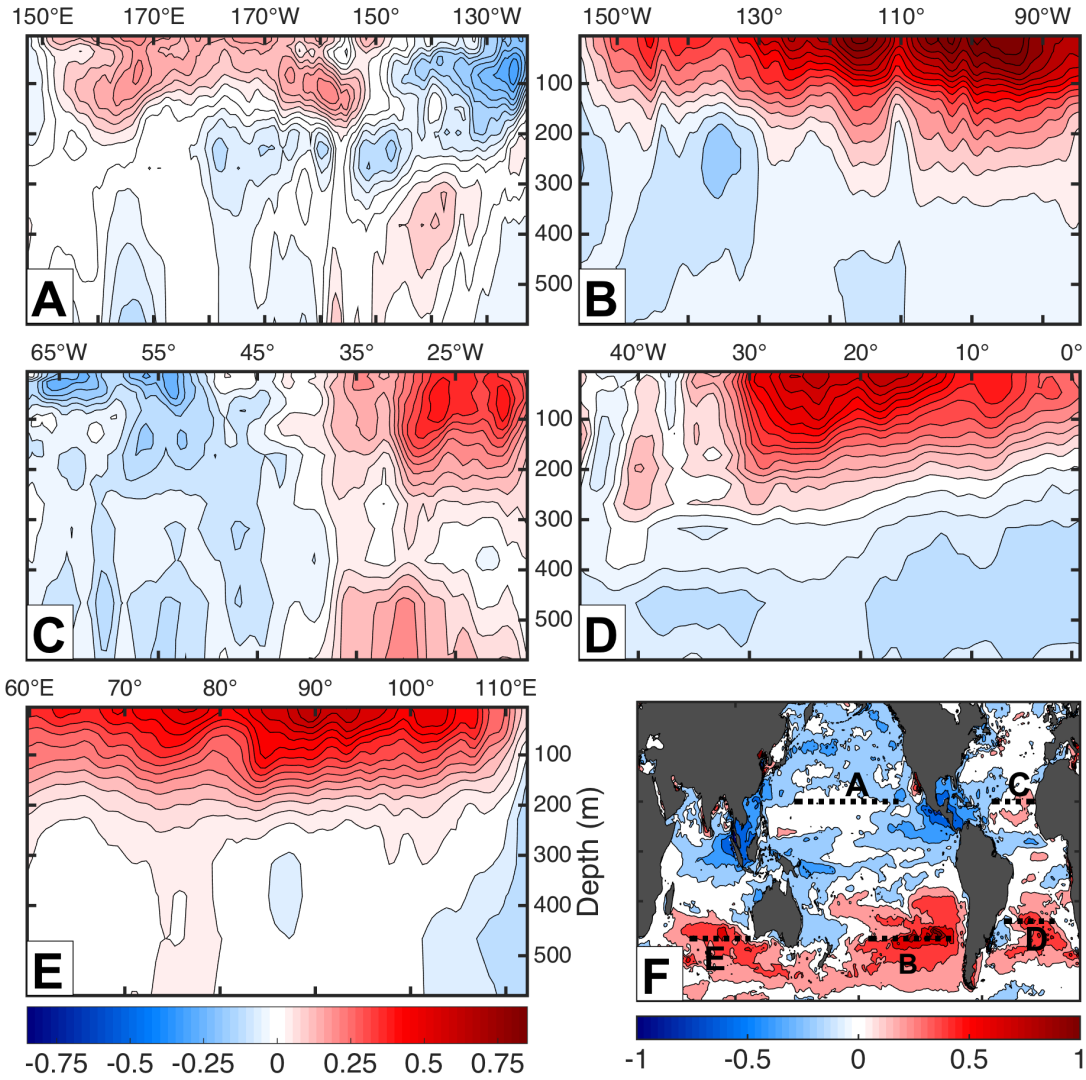

Figure 3.11: (a-e) Longitude-depth transects of 1950-2008 linear salinity trend from SODA to a maximum of 500 m depth [psu]. The colorbar south of (e) applies to panels (a)-(e). (f) Map of multidecadal linear SSS trend [psu] from 60°N-60°S. Dotted lines indicate profile sections taken in (a)-(e), corresponding to positive SSS trend from SODA.

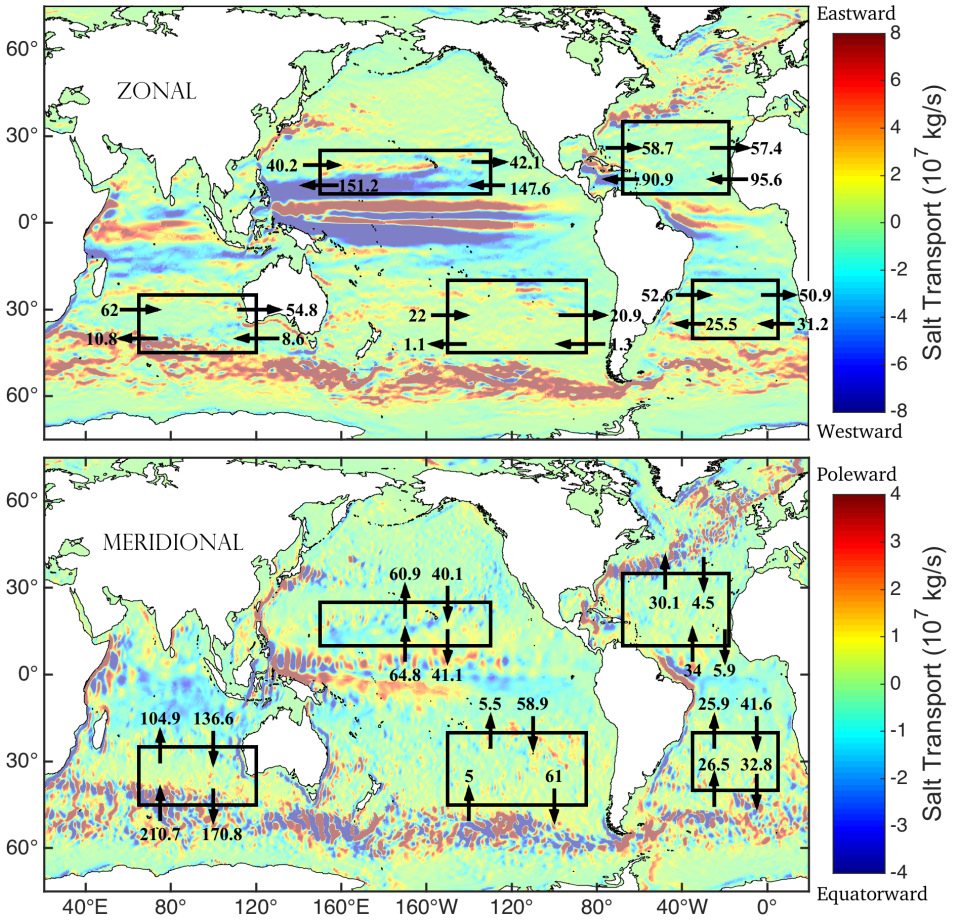

Figure 3.12: Climatological mixed layer salt transport in the (a) meridional and (b) zonal directions from SODA reanalysis. Arrows denote vertically integrated fluxes across the indicated bounds of the outlined boxes (10^7 kg s^{-1}). Note that the absolute direction of motion is reversed in the color scheme at the equator in the meridional subplot, as well as the fact that fluxes at the surface and base of the mixed layer are not constrained.

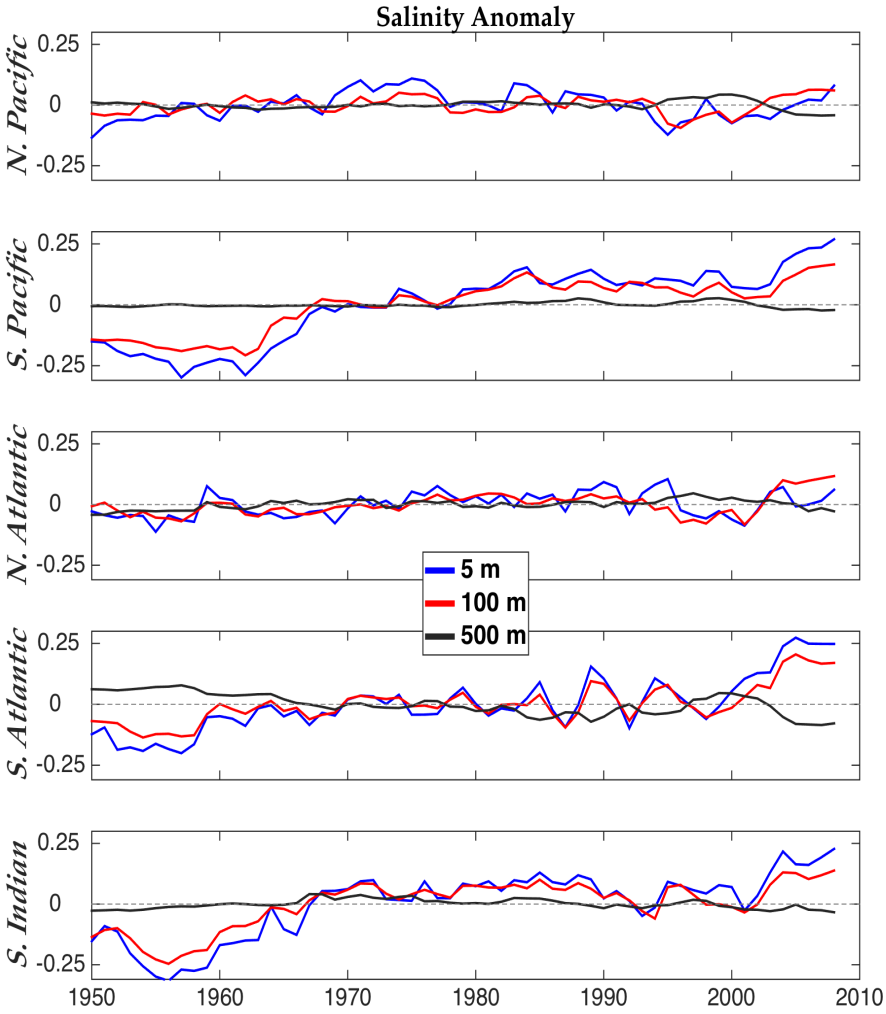

Figure 3.13: Multidecadal time series of salinity [psu] anomalies from the climatological mean in the a) subtropical North Pacific, b) subtropical South Pacific, c) subtropical North Atlantic, d) subtropical South Atlantic, and e) subtropical South Indian subtropical gyre at 5m, 100m, and 500m depth from SODA reanalysis.

CHAPTER 4

[4]EVALUATION OF GRACE MASCON GRAVITY SOLUTION WITH RELATION TO INTERANNUAL OCEANIC WATER MASS VARIATIONS

[4]Melzer, B. A., and B. Subrahmanyam. 2016. Evaluation of GRACE Mascon gravity solution with relation to interannual oceanic water mass variations. Submitted to *Transactions on Geoscience and Remote Sensing*.

Abstract- With evidence of an accelerated water cycle over the past few decades, we make inferences on the spatial variability of interannual evaporation and precipitation patterns from 2003-2014 gravity anomalies, using the Gravity Recovery and Climate Experiment (GRACE) satellite mascon dataset. Comparison of the mascon solution to an ensemble harmonic solution is conducted, along with validation over the oceans via sea surface height from multi-mission altimetry minus Argo floats data/GECCO2 (the GECCO2 ocean synthesis is the German contribution of the Estimating the Circulation and Climate of the Ocean project (ECCO, www.ecco-group.org)) steric height. The mascon solution was consistently more accurate than its spherical harmonic counterpart across large spatial and temporal scales, due mainly to the inherent smoothing from the mascon cells. Comparison of GRACE to both GECCO2 + altimetry and Argo + altimetry mass estimates revealed an offset in phase with regards to the annual cycle, but yielded an rmse of only 5.6 mm in the interannual signal after phase correction. This study furthers evidence of an accelerated water cycle at a rate of 1.5 ± 1.1% at low latitudes, and also provides a means of validation for oceanic freshwater budget studies based upon salinity measurements.

4.1. Introduction

The global water cycle is expected to have intensified as a response to anthropogenic global warming [*Skliris et al.,* 2014; *Durack et al.,* 2012; *Helm et al.,* 2010], since the capacity of air to hold and distribute moisture is dependent on temperature, a relationship that has been parameterized by the Clausius-Clapeyron relation [*Held and Soden,* 2006]. For this reason, the focus of many has become that of estimating freshwater fluxes over the oceans, which account for 86% of global evaporation and 78% of global precipitation [*Ren et al*., 2014]. Direct measurements of evaporation and precipitation remain spotty, but freshwater fluxes over the air-sea interface can be inferred from other proxies that are better resolved over the global ocean.

The introduction of satellite observations to our global monitoring system has given us a synoptic view of the oceans, allowing us to expand our knowledge of the water cycle beyond the regional variability that we have previously been limited to. The NASA Aquarius salinity mission, launched in 2009, and Gravity Recovery and Climate Experiment (GRACE), launched in 2002, are both vital to diagnosing changes to the global water cycle. The recently launched Aquarius satellite can measure the distribution of sea surface salinity, which is commonly used as a proxy to convey areas of high or low precipitation over the oceans [*Durack et al.,* 2012]. GRACE satellite can measure gravity anomalies from the earth's geoid. From these gravity anomalies we can infer mass variations on the earth's surface between orbit passes, of which water redistribution is the dominant signature.

In this paper, we will focus on GRACE, which can track both oceanic and terrestrial changes in water storage over time through measurements of the Earth's gravity field.

With early processing techniques, there was no GRACE product with the precision necessary to study basin and global scale mass variability. This is particularly apparent on the interannual level, where *Anderson and Hinderer* [2005] has reported a modest accuracy of 9 mm equivalent water thickness (EWT) in groundwater storage over large spatial scales. However, mass fluxes over the oceans require much greater accuracy, as they are on the order of only a few millimeters EWT in magnitude as compared to several centimeters in terrestrial systems. Harmonic GRACE solutions have been shown to significantly underestimate the rate of ocean mass increase as cross validated with Jason and Argo estimates [*Willis et al.,*2008]. With the recently developed mascon solution, we now have increased capability in detecting minute signals over the oceans, which collectively hold a significant contribution towards the closure of the global mass budget and also the observed regional sea level rise [*Watkins et al.,* 2015].

Furthermore, there are significant periodicities in interannual water storage that have made it difficult to isolate climate related trends given the length of the GRACE mission. This includes frequencies which are coherent with ENSO [*Güntner et al.,* 2007] and also with North Atlantic Oscillation (NAO) [*Labat,* 2007] over both oceans and continental watersheds. *Schmidt et al.* [2008] has shown that these periodicities are also consistent with GRACE data. With nearly 13 years of GRACE observations, we now have enough data to begin to filter out these fluctuations and diagnose the underlying climate scale trend freshwater distribution, which is believed to be a quadratic in regions like the Greenland and Antarctic ice sheets [*Velicogna,* 2009]. A quadratic relationship would imply a constant acceleration of these trends in the past 5 years, and thus we wish to

analyze this trend through 2014 with the understanding that GRACE gravity anomalies would be amplified and slightly easier to detect under such a trend.

Quantifying trends in fluxes of water over both land and ocean can also serve to further our knowledge of the components that contribute to sea level rise, as we can generally only see the sum of all contributors through altimetry. Because altimeters can only resolve sea level anomalies over the oceans, GRACE data is valuable in determining the source regions of freshwater input to the oceans, and also in monitoring the fluxes over the land-sea interface, which includes glacial input and river discharge.

4.2. Data/Methods

4.2.1 Ocean mass variations inferred from GRACE Gravimetry

The Gravity Recovery and Climate Experiment (GRACE) consists of two identical satellites that map the Earth's gravity field by measuring the distance between the two satellites at any given point in time. From the gravity field, we can derive variations of mass within Earth on 30-day intervals, namely the storage of surface water, soil moisture, groundwater, and snow. These reservoirs are controlled by the regional rates of precipitation, evapotranspiration, and net river flow [*Ramillien and Bunau,* 2004]. The horizontally and vertically integrated quantities obtained from GRACE make it suitable for water budget studies and also for tracking losses in glacial mass and associated sea level rise [*Rodell et al.,* 2004]. We will achieve this through the comparison of GRACE with observed and steric sea surface height anomalies. Two different gridded mass products (spherical harmonic vs mascon) will be examined to provide detail on the

performance of each with relation to the global water cycle, as briefly addressed by [*Watkins et al.,* 2015].

For the harmonic solution, we calculate an ensemble mean of the JPL, CSR, and GFZ Level 3 harmonic products [*Wiese*, 2015] as suggested by *Sakumura et al.* [2014]. The gridded 1° x 1° product is based on spherical harmonics, and is processed to include GIA correction, atmospheric correction, destriping, and smoothing. The difficulty in detection of water cycle trends from GRACE lies in alternate modes of mass redistribution, including postglacial rebound [*Schmidt et al.,* 2008] and major earthquake events [*Han et al.,* 2006]. Glacial isostatic adjustment (GIA) corrections applied to the data are based on the model given by [*Geruo et al.,* 2012]. The overall rmse of GRACE observations is on the order of a few millimeters equivalent water thickness (EWT) [*Swenson and Wahr,* 2002], with the highest uncertainty associated with variability in snow cover, soil moisture, and groundwater reservoirs [*Ramillien and Bunau,* 2004].

We will compare the harmonic solution to the recently developed GRCTellus/JPL spherical cap mass concentration (mascon) product v2.0. This breaks the Earth's surface into blocks of water (mascons), for which the mass contained is solved explicitly. The mascon gravity fields provide a lower rmse and higher resolution than spherical harmonic solutions, with less processing required to filter out stripes and derive scaling factors in the post processing stages. This data is gridded to ½° x ½° with a native resolution composed of 3° x 3° equal area mascon cells. Coastal cells have been treated with a Coastline Resolution Improvement (CRI) filter to accurately distinguish between land and ocean portions of mascon cells which envelop both. From here we applied a set of scaling factors over the land as suggested by *Watkins et al.* [2015], and applied a 300 km

Gaussian filter to smooth the data. Cells within 500 km of the coastline were masked prior to filtering to avoid leakage effects, which would otherwise dominate the signal of coastal waters since the signal over land can be up to five times greater in magnitude than the ocean.

Starting in 2011, temporal gaps exist in both sets of data (about 2-3 months/yr, see http://isdc.gfz-potsdam.de/index.php?name=News&file=article&sid=170 for details) where the instruments were switched off in order to conserve battery health and extend the mission. When necessary for computing yearly averages, these missing months were filled in using a shape-preserving interpolation in order to preserve the length of the time series, but also leading to an increased uncertainty in the recent few years.

4.2.2 Ocean mass variations inferred from sea level

Interannual sea level anomalies (SLA) are attributed to two primary modes: density variability and mass fluxes. The former can be quantified through steric sea level calculations from Argo and GECCO2 salinity and temperature. By removing the steric sea level trend from the observed trend (via altimetry), we obtain estimates of freshwater fluxes, which can be compared to GRACE mass observations over the global ocean. This method has been employed by *Llovel et al.* [2010] and others, with relative success. Some of their large error estimates in this method were believed to be embedded in the spatial coverage of Argo profiles along with possible deep ocean variability, which we will attempt to resolve by incorporating a reanalysis dataset into the analysis.

4.2.2.1 Argo CTD profiles

Argo temperature and salinity profiles are assimilated into global monthly-averaged data sets by the International Pacific Research Center (IPRC), University of Hawaii, spanning from 2005 to 2015. *Riser et al.* [2008] has reported a global salinity error of 0.01 psu from recovered floats. Because of relatively low global float density, the IPRC uses optimal interpolation to produce a final 1° × 1° gridded product. We have chosen to interpolate the IPRC product from 27 to 52 standard vertical levels with a maximum depth of 2000 m.

4.2.2.2 GECCO2 temperature and salinity reanalysis

GECCO2 is the German contribution to the Estimating the Circulation and Climate of the Ocean (ECCO) project, part of the World Ocean Circulation Experiment (WOCE). As the 2000 m vertical range of Argo does not span the entire water column, we utilize GECCO2 reanalysis in order to estimate lower frequency changes beyond the range of Argo, which may also contribute to steric changes. Additionally, Argo floats do not penetrate the polar regions, which makes it imperative to utilize GECCO2 in this analysis, as GECCO2 includes a dynamic/thermodynamic sea ice model [*Köhl,* 2014]. The GECCO2 monthly reanalysis products are available at a resolution of 1°x1°, with 50 vertical levels extending to a depth of 6000 m when applicable. The reanalysis uses the MIT global circulation model, and receives inputs from CTD, XBT, Argo, and satellite observations.

4.2.2.3 Ocean Steric height methodology

Steric calculations were based on the following relation [*Kusche et al.,* 2016],

$$\eta(\lambda,\theta,t) = \int_D^0 \frac{1}{\rho_0(z)}[\rho(\lambda,\theta,z,t) - \bar{\rho}(\lambda,\theta,z)]dz, \qquad (4.1)$$

where ρ is the density as a function of temperature and absolute salinity. ρ_o is the density of standard seawater at the given depth *z.* The calculation was performed point by point using the Gibbs Seawater Oceanographic Toolbox v3.05, developed by SCOR/IAPSO Working Group 127 [*McDougall and Barker,* 2011].

4.2.2.4 Mean Sea Level Anomalies from all-sat merged Altimetry product

The Ssalto/Duacs multimission mean sea level anomaly (MSLA) product is an ensemble of all complimentary satellite altimeters available, utilizing combinations of Topex/Poseidon, Jason-1, Envisat, GFO, Jason-2, and Cryosat-2 altimeters. The relative contribution of each satellite across time is determined through a DFS analysis [*Dibarboure et al.,* 2011]. The top two contributors are the Jason-2 and AltiKa missions. We use the gridded monthly dataset, with a resolution of ½° x ½°, spanning from 2002-2015. Interannual sea level anomalies (SLA) are attributed to two primary modes: density variability and mass fluxes. The former can be quantified through the above steric calculations from Argo and GECCO2. By removing sea level rise due to steric effects, we obtain estimates of freshwater fluxes, which can be compared to GRACE mass observations over the global ocean.

4.3. Results

First we take a look at the intraannual mass variability over the globe using the GRACE mascon product (Figure 4.1), as the regions with the largest seasonal cycle of rainfall are most sensitive to climate scale variability as well. The Amazon Basin, Congo Basin, and Indian Basin all receive large amounts of rainfall during the wet season, with this rainfall contributing to the soil moisture, groundwater, and high river discharge into the ocean during these times. The oceanic subtropical gyres show nearly no change in mass over intra-annual timescales, while the subpolar latitudes have up to 12 cm EWT imported and exported in a year, with a net change near zero. This is largely due to the high precipitation rates in these regions, as well as the seasonal thawing and refreezing of ice sheets. The global ocean has a seasonal amplitude of 6.5 mm EWT, slightly lower than the 6.8 mm value obtained from Argo and Jason-1 [*Willis et al.,* 2008].

After removing this seasonal cycle from the signal, we can see the net mass flux (Figure 4.2a). The global mean change in mass over the continents is -3.12 mm EWT yr^{-1}. The areas showing consistent negative mass flux are the Greenland region, Siberian, and Central European regions. These locations are all characterized by retreating snow/ice cover due to global warming [*Ramillien et al.,* 2006], [*Romanovsky et al.,* 2010]. As previously documented by *Ramillien et al.* [2006], the Antarctic continent shows a clear bimodal pattern, with the western side of the landmass losing mass and the eastern side gaining mass. Areas that are receiving a yearly influx of freshwater mass include the Amazon basin and East Australia, areas which house tropical or temperate rainforests. In contrast, the deserts of the world, namely the North American and North African deserts, are getting progressively drier over time. We note that the bulk of mass

lost is from polar (> 60°) latitudes, while tropical latitudes (< 30°) are gaining in mass. Thus, there is an inter-annual trend in equatorward movement of freshwater.

The uncertainty of the monthly mascon solution is provided in Figure 4.2b, with a global value of 16 mm EWT. As expected, the greatest uncertainty is associated with the regions of large seasonal cycle, with uncertainty as high as 65 mm EWT within the Amazon basin. Evaluating the difference between the GRACE mascon and harmonic mass solutions, we obtain a global difference of 3.2 mm EWT, with the variability as high as 10 mm in Greenland and along the Gulf of Alaska. The most significant difference is present over Greenland, where the mascon estimation is lower than the harmonic along the western boundary of the landmass and higher along the central portion (Figure 4.2c). There is an apparent overestimation of the harmonic solution in the Southern Ocean, and an underestimation in the north Pacific.

Since the oceans account for the bulk of evaporation and precipitation over the globe, we will focus on the oceanic fluxes, as they are far less resolved than their terrestrial counterparts. Moreover, further validation is also available from the altimetric-steric approach. We compare the observed trends of GRACE to those from coupled satellite altimetry and Argo/GECCO2, as these sources have been providing us with accurate observations even before the launch of the GRACE mission in 2002. First, we analyze the steric sea level changes obtained from Argo temperature and salinity profiles. A positive steric SSH trend is present over nearly the entire global ocean, attributed to thermal expansion, with the notable exception of the western boundary currents in the Pacific and Indian oceans (Figure 4.2c). There is a negative steric trend along the front between the Kuroshio extension and recirculation gyre of the west Pacific, reflective of the high

interannual and decadal variability in the strength of the recirculation gyre and mesoscale eddies that are shed in the region [*Qiu and Chen,* 2005]. This could be related to an intensification of the Kuroshio current system driven by increasing temperatures, as the rate of surface warming in this region is known to be two to three times faster than the global mean [*Wu et al.,* 2012].

Following removal of the steric trend, we obtain the estimated mass variation over the oceans from altimetry (Figure 4.3). The mascon product shows good coherence with mass change estimates using both observational Argo data and GECCO2 reanalysis, with rmse values of 8.7 mm and 7.8 mm EWT, respectively. One contribution to the mascon rmse is the apparent phase lag that is present in the seasonal max and min of nearly every year, with the mascon solution peaking approximately two months early (Figure 4.4). We interpret this as a lag in the Argo/GECCO2 profiling data, as the primary mechanisms of steric sea level, diffusion and advection, may explain the delayed response, particularly at deeper levels [*Piecuch and Ponte,* 2011]. This has previously been observed and the top two modes addressed through EOF analysis [*Chambers,* 2006], so we will not dwell on it. The phase corrected rmse values are 6.5 mm and 5.6 mm EWT. This is 75-89% less error than the harmonic solution. The global mean mass change from altimetry is +3.56 mm EWT yr^{-1}, as compared to +3.12 mm yr^{-1} estimated by GRACE. Both altimetry and gravimetry estimates show an increase in oceanic water mass on the order of a few millimeters, in agreement with the findings of *Cazenave et al.* [2009]. The 0.44 $mmyr^{-1}$ difference can be attributed to several sources of ambiguity. Argo float density remains relatively low in some regions, and the gridded product is missing data in key regions such as those in the Indonesian Throughflow region and at latitudes > 50°. GIA

adjustment appears to remain the primary source of error for GRACE measurements, as the true magnitude of the glacial rebound rate is still up for debate [*Riva et al.,* 2009].

Analyzing the mascon solution on a synoptic level, we note that the loss of mass over the continents is compensated by an addition of mass to the global ocean. We also note that the change in oceanic freshwater import/export shows a spatial coherence with latitude (Fig. 5). The high rate of freshwater input at 80°N reflects the heavy runoff and glacial retreat around the subcontinent of Greenland. Despite the bimodal tendency of Antarctica, the region is experiencing a mean decrease in mass (Fig. 6), implying that the rate of volume loss in the west dominates the rate of volume gain in the east on interannual time scales. As a whole, Greenland and Antarctica are decreasing in mass at average rates of 3.2 cm (359 Gt) yr^{-1} and 2.5 cm (282 Gt) yr^{-1}, respectively. Our calculated rate of mass export in both regions is 12% greater in Greenland than previous estimates (2006-2009) given by and [*van den Broeke et al.,* 2009] from GRACE via spherical harmonic processing. This is in agreement with the trend acceleration noted by [*Velicogna,* 2009]. Taking the same calculation with proportion to surface area indicates that the rate of mass export over Greenland per unit area is 536% greater than Antarctica.

From a qualitative perspective, we see trends that support previous observations of the oceanic branch of the global water cycle, despite the integration of all basins in our analysis. There is a net loss of mass in the subtropics of both hemispheres, with the rate in the southern hemisphere peaking around 30°S, and the northern hemisphere peaking around 40°N. These latitudes correspond to the regions along the poleward boundaries of the subtropical gyres, which are under a positive trend in decadal sea surface salinity, and thus believed to show a positive imbalance in evaporation-precipitation [*Durack,* 2015].

There also exists a peak in the rate of mass gain under the mean location (8°N) of the Inter Tropical Convergence Zone (ITCZ), suggesting that the interannual precipitation under the ITCZ is increasing as well. This provides observational data to support the reanalysis results of [*Gu et al,* 2007], which found a 5.5% increase in precipitation in the tropical oceans over 12 years. While we also observe an increase in mass, our estimate is more conservative at 1.5 ± 1.1% between 20°S and 20°N over the same span. This calculation is performed under the assumption that there is no loss of mass due to circulation, which could contribute to the observed mass change.

4.4. Discussion

The mascon approach to processing gravity anomalies from GRACE shows much better agreement with decomposed sea level data than the spherical harmonic solution on the basin to global scale, with a global uncertainty of 1.6 cm, and 1.1 cm over the oceans. This is a result of the higher signal/noise ratio and reduced post-processing in the mascon method, which allows for lower scaling factors and less potential for error due to the inherent smoothing of the mascon cells. The implementation of the coastline improvement filter also significantly reduces leakage along the land-sea interface, where oceanic gravity anomalies have generally been overestimated in past data products. Despite the interannual agreement of GRACE mascon data with Argo and altimetry, we capture a significant two-month phase offset of the annual cycle. The lower phase of GRACE over the oceans relative to altimetry estimates is actually disparate of the phase lag found over terrestrial water sheds [*Chen et al.,* 2005], but in agreement with the findings of *Chambers* [2006] in the oceanic regime. Future studies may seek to expand

our preliminary results in combining land and sea measurements for a global mass balance, as validation in this regard is quite difficult.

With regards to Argo and GECCO, there is a disparity in the magnitude of the seasonal cycle (Argo is consistently 8.7 mm greater), but the interannual trend does not appear to show a significant difference between the two products. Thus, it is suggested that the potential temperature and salinity below 200 m depth can be assumed negligible for calculations of steric height trends over time spans up to a decade. Consequently, this analysis strengthens the validity of sea level change results obtained from global Argo profiles, including interannual studies such as [*Willis et al.,* 2008]. The discrepancy between altimetry and gravimetry measurements suggests that steric changes in sea surface height account for approximately 50% of observed yearly sea level rise.

As our direct observation system of evaporation and precipitation is sparse over the oceans, we have shown that this important branch of the water cycle can be estimated indirectly from satellite, which provides us with unprecedented spatial and temporal resolution over unmonitored regions of the world ocean. The interannual spatial trends in GRACE indicates that dry areas are getting drier, while wet areas are getting wetter over time. This supports the forecast of increased contrast between geographical areas as suggested by *Durack et al.* [2012]. Our results from satellite gravimetry points to an intensification of the global water cycle at an average rate of 1.25% per decade, a trend consistent with previous GRACE [*Velicogna,* 2009] and salinity-derived evidence [*Skliris et al.,* 2014; *Durack et al.,* 2012; *Helm et al.,* 2010] as well as our direct estimate obtained from sea level observations. As expected, regions of large annual cycle also showed the highest interannual trend, regardless of the sign. We suggest that with respect

to latitude, oceanic water storage does indeed provide evidence for an intensification of the water cycle based on trends in the tropics and subtropics. Additional synthesis would be required if we wish to use GRACE to quantify the relative contribution of the E-P trend to mass variation in polar and subpolar regions, assuming such a trend exists as suggested by *Dyurgerov* [2003] and *Huntington* [2006].

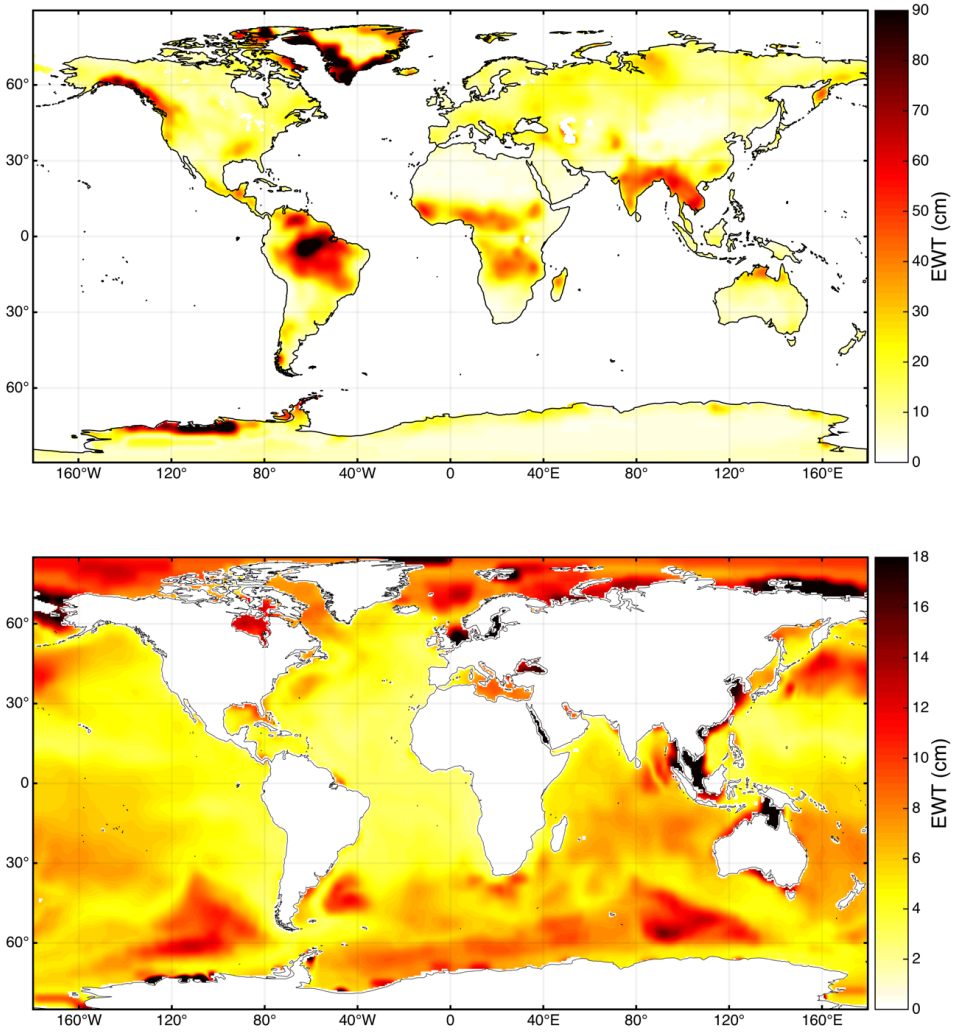

Figure 4.1: Amplitude of seasonal terrestrial (top) and oceanic (bottom) mass variation from GRACE [cm].

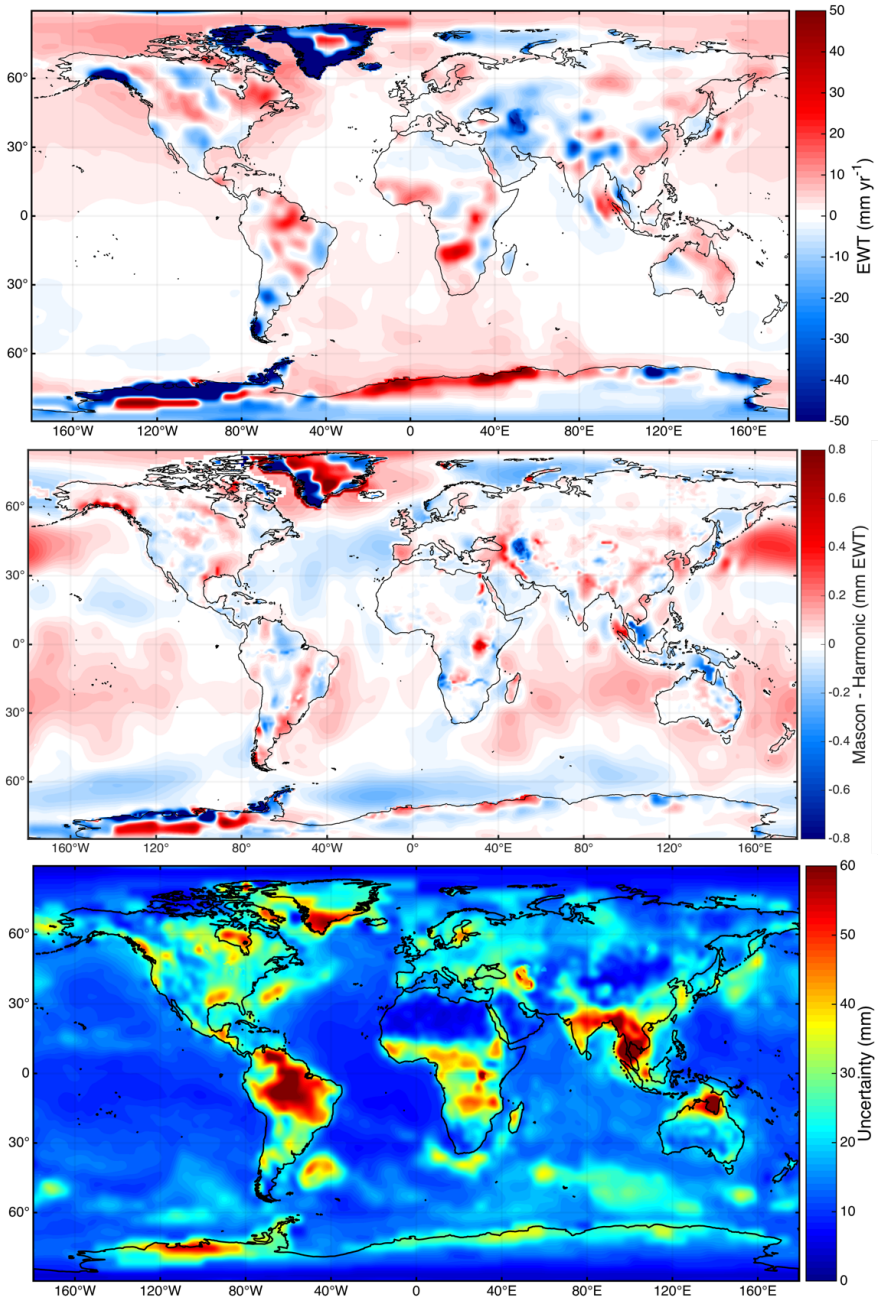

Figure 4.2: (top) 2003-2015 mass flux from GRACE mascon solution [mm yr^{-1}], (middle) monthly difference between the JPL mascon and composite harmonic mass grids (mascon-harmonic) derived from GRACE [mm EWT], (bottom) uncertainty in GRACE mascon solution [mm EWT].

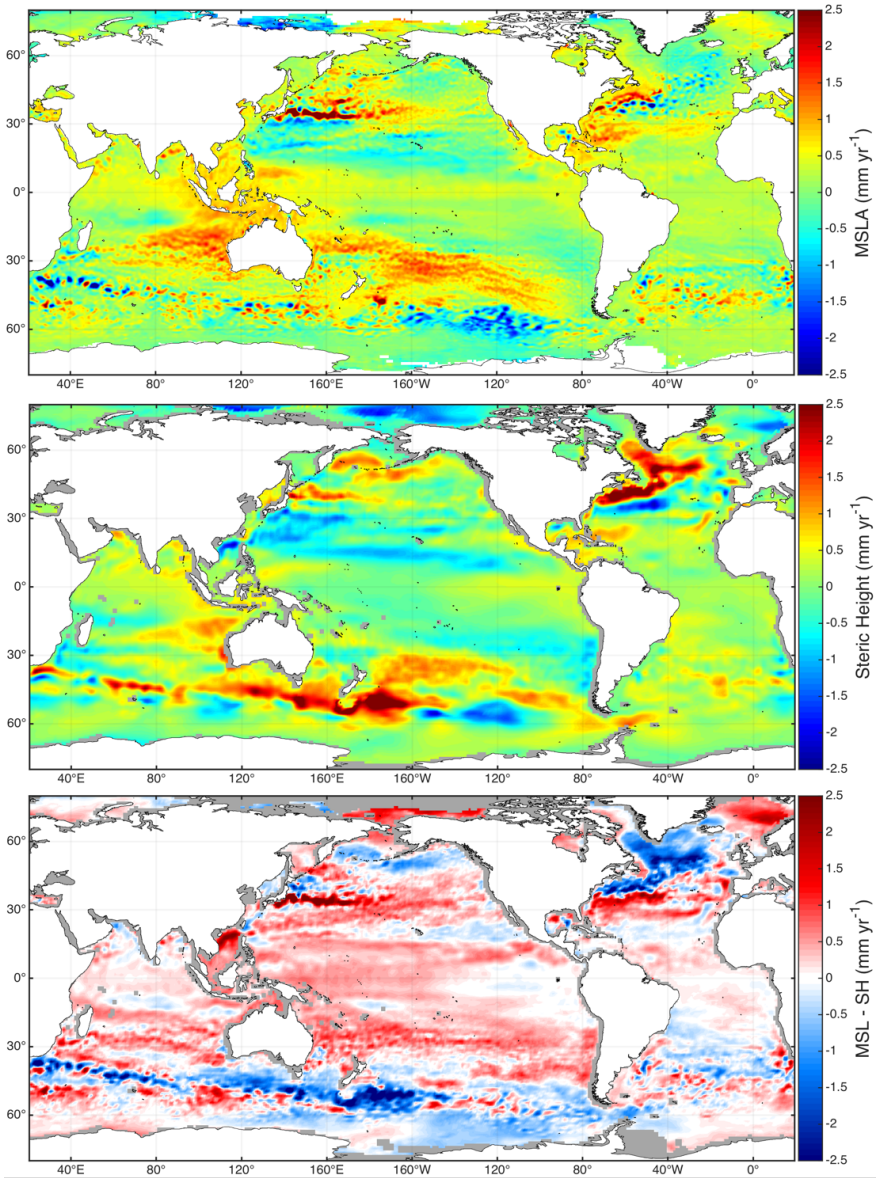

Figure 4.3: 2003-2014 (top) annual change in sea surface height (SSH) from altimetry, (middle) annual change in steric sea surface height (SH) from GECCO2, (bottom) residual sea surface height anomaly (SSH-SH) over the global oceans [mm yr^{-1}].

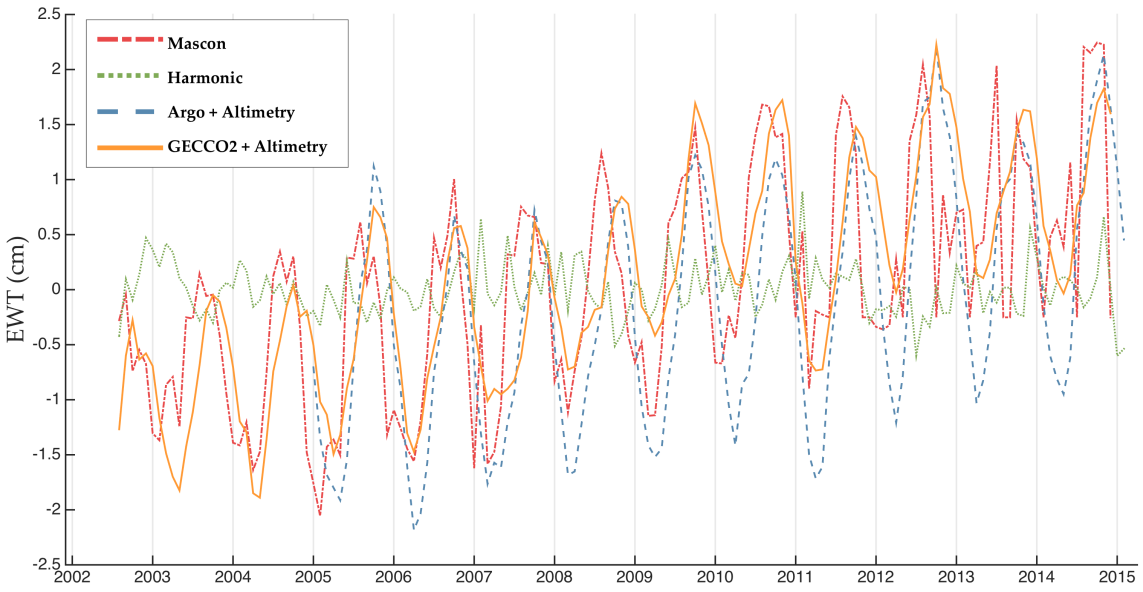

Figure 4.4: 2002-2015 Monthly mass anomalies [cm EWT] over the global ocean from GRACE Mascon solution (red), GRACE harmonic solution (green), altimetry corrected with Argo computed steric height (blue), and altimetry corrected with GECCO2 computed steric height (orange).

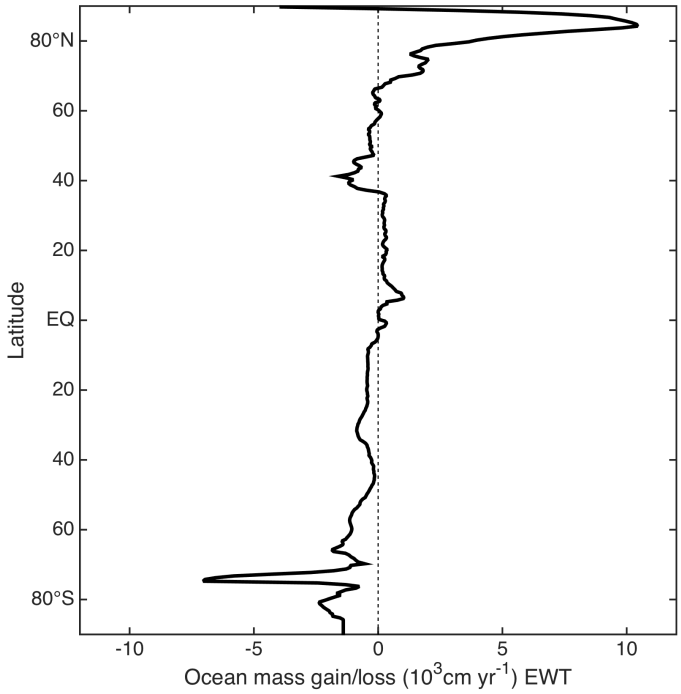

Figure 4.5: Rate of global oceanic mass change as a function of latitude [10^3 cm yr^{-1} EWT].

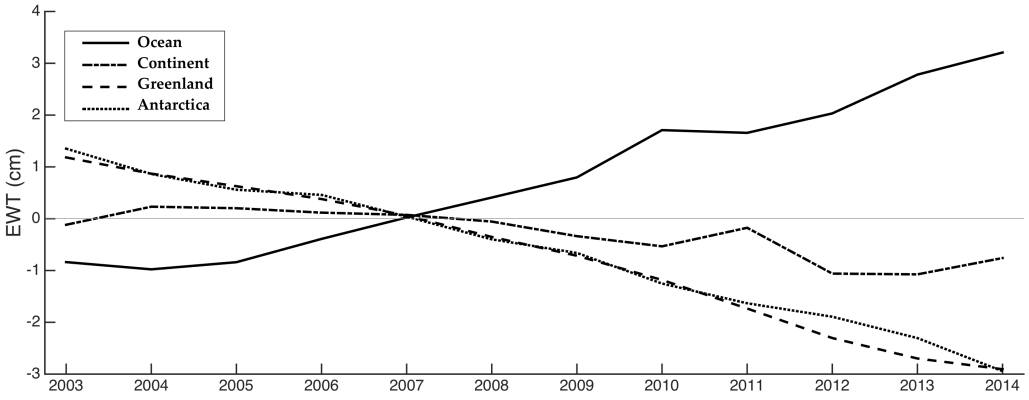

Figure 4.6: Large scale mass anomalies over each of the major global water reservoirs [cm EWT].

CHAPTER 5

CONCLUSIONS

The focus of this thesis has been to diagnose and quantify the observed intensification of the global water cycle through implementation and cross-validation of three different E-P proxies for the oceans on interannual to decadal timescales. We determined that sea surface salinity is the most consistent parameter, and also the most promising for future studies of this topic, as the dawn of satellite-derived salinity is now providing us with better coverage than ever before.

Chapter 2 utilizes the known relationship between SSS and E-P to infer global water cycle intensification from salinity trends in the remote subtropical gyre regions. We also showed that the Aquarius and SMOS satellites are both within 0.2 psu error in the subtropical gyres, while providing observations at much greater spatial resolution than in situ Argo salinity fields. An average salinity increase of 0.12 psu was revealed in the subtropical gyres, with the greatest increase located in the South Pacific gyre. In addition, a zonal gyre drift was also observed in the North Atlantic, South Pacific, and South Indian gyres at rates of up to 24 km/yr after removing oscillations associated with Pacific Decadal Oscillation (PDO) and Atlantic MultiDecadal Oscillation (AMO).

Chapter 3 explored subsurface salinity trends in the subtropical gyres to determine the contribution of lesser factors to the observed surface trends which we previously attributed to decadal E-P changes. Consistent with the findings of Chapter 2, we observed a depth-diminishing increase in subtropical gyre salinity to a depth of 200 m, at which point all regions shift to a slight freshening trend. The regions where a positive salinity trend is present are located to the south of the salinity maximum of each subtropical gyre. Construction of a mixed layer salinity budget reveals an increase in the transport of salt into and out of all study regions, of with the meridional component accounting for a greater portion of this trend. This suggests that there is an increase in net evaporation in both the study regions and the E-P maxima at lower latitudes in each basin.

Chapter 4 introduces an alternative method to viewing the global water cycle through GRACE gravity anomalies. Estimating the redistribution of freshwater with GRACE is a good way to integrate oceanic and continental observations of freshwater exchanges between the major reservoirs, as these two components are generally studied as independent systems. Specifically, we show here that the mascon processing solution is more accurate and of higher resolution over the oceans than the spherical harmonic processing solution. This allows us to finally begin to apply GRACE observations to the oceans with some degree of confidence, where freshwater fluxes are generally much smaller than over land. Comparison of GRACE mass anomalies to sea surface height derived anomalies provides further validation of its potential with regards to the global water cycle, although the underlying issue in polar regions is quantifying and removing oceanic mass anomalies that are attributed to sea ice extent/retreat.

The results presented in this thesis are robust in their agreement with prior global studies of the global water cycle, and provide implications to the E-P patterns of the tropical and polar latitudes, as any loss in subtropical freshwater mass must be compensated by a remote addition of mass through atmospheric pathways. Additional validation of our results from Simple Ocean Data Assimilation (SODA) reanalysis may be achieved through an analysis which utilizes other reanalysis products such as European Center for Medium-Range Weather Forecasts (ECMWF) reanalysis or German Contribution of the Estimating the Circulation and Climate of the Ocean Project (GECCO2). Pertaining to sea surface salinity as a proxy for E-P, the recent launch of the Soil Moisture Active Passive (SMAP) satellite by NASA in 2015 will be instrumental in improving our understanding of synoptic and mesoscale salinity processes by providing observations with a global coverage every 8 days at an unprecedented spatial resolution of 40 km to compliment the ever-growing array of Argo floats in the global ocean. To conclude, we should continue to utilize satellite derived salinity observations in our studies of the global water cycle, as our knowledge and observational infrastructure of ocean salinity is rapidly expanding.

REFERENCES

Anderson, O. B., and J. Hinderer (2005), Global inter-annual gravity changes from GRACE: Early results, *Geophys. Res. Lett., 32*(1).

Bakun, A. (1990), Global climate change and intensification of coastal ocean upwelling. *Science, 247*(4939), 198-201.

Bakun, A., D. Field, A. Redondo-Rodriguez, S. J. Weeks (2010), Greenhouse gas, upwelling-favorable winds, and the future of coastal ocean upwelling ecosystems, *Global Change Biology*, 16, 1213-1228.

Balmaseda, M., D. Anderson, and A. Vidard (2007), Impact of Argo on analyses of the global ocean, *Geophys. Res. Lett., 34*(16).

Bauer, E., and G. Siedler (1988), The relative contributions of advection and isopycnal and diapycnal mixing below the subtropical salinity maximum, *Deep Sea Res., 35*(5), 811-837.

Bryden, H. L., H. R. Longworth, and S.A. Cunningham (2005), Slowing of the Atlantic meridional overturning circulation at 25 N. *Nature*, *438*(7068), 655-657.

Carton, J. A., and B. S. Giese (2008), A reanalysis of ocean climate using Simple Ocean Data Assimilation (SODA), *Mon. Wea. Rev.*, *136(8),* 2999-3017.

Carton, J. A., G. Chepurin, and X. Cao (2000), A simple ocean data assimilation analysis of the global upper ocean 1950-95. Part II: Results, *J. Phys. Oceanography*, *30*(2), 311-326.

Cazenave, A., K. Dominh, S. Guinehut, E. Berthier, W. Llovel, G. Ramillien, ... & G. Larnicol, (2009), Sea level budget over 2003–2008: A reevaluation from GRACE space gravimetry, satellite altimetry and Argo, *Global and Planetary Change, 65*(1), 83-88.

Chambers, D. P. (2006), Observing seasonal steric sea level variations with GRACE and satellite altimetry. *J. Geophys. Res. Oceans, 111*(C3).

Chen, J. L., M. Rodell, C. R. Wilson, J. S. Famiglietti (2005), Low degree spherical harmonic influences on Gravity Recovery and Climate Experiment (GRACE) water storage estimates, *Geophys. Res. Lett., 32*(14).

Cunningham, S. A., T. Kanzow, D. Rayner, M. O. Baringer, W. E. Johns, J. Marotzke, … and H. L. Bryden (2007), Temporal variability of the Atlantic meridional overturning circulation at 26.5 N., S*cience*, *317*(5840), 935-938.

Curry, R., B. Dickson, and I. Yashayaev (2003), A change in the freshwater balance of the Atlantic Ocean over the past four decades. *Nature, 426*(6968), 826-829.

Di Lorenzo, E., et al. (2009), Nutrient and salinity decadal variations in the central and eastern North Pacific, *Geophys. Res. Lett*., *36*(14).

Dibarboure, G., M. I. Pujol, F. Briol, P. L. Traon, G. Larnicol, N. Picot, … and M. Ablain (2011), Jason-2 in DUACS: Updated system description, first tandem results and impact on processing and products, *Marine Geodesy, 34*(3-4), 214-241.

Dong, S., G. Goni, and R. Lumpkin (2015), Mixed-Layer Salinity Budget in the SPURS Region on Seasonal to Interannual Time Scales, *Oceanography, 28*(1), 78-85.

Drucker, R., and S. Riser (2014), Validation of Aquarius sea surface salinity with Argo: Analysis of error due to depth of measurement and vertical salinity stratification, *J. Geophys. Res., 119*(7)*,* 4626-4637.

Durack, P. J. (2015), Ocean salinity and the global water cycle. *Oceanography, 28*(1), 20-31.

Durack, P. J., and S. E. Wijffels (2010), Fifty-year trends in global ocean salinities and their relationship to broad-scale warming, *J. Clim., 23*(16), 4342-4362.

Durack, P. J., S. E. Wijffels, and R. J. Matear (2012), Ocean salinities reveal strong global water cycle intensification during 1950 to 2000, S*cience*, *336*(6080), 455-458.

Dyurgerov, M. (2003), Mountain and subpolar glaciers show an increase in sensitivity to climate warming and intensification of the water cycle, *J. Hydrology, 282*(1), 164-176.

Fang, F., and R. Morrow (2003), Evolution, movement and decay of warm-core Leeuwin Current eddies, *Deep-Sea Research II*, *50*, 2245-2261.

Feng, M., M. J. McPhaden, S.P. Xie, and J. Hafner (2013), La Niña forces unprecedented Leeuwin Current warming in 2011, *Scientific Reports*, *3*, 1277.

Foltz, G. R., and M. J. McPhaden (2008), Seasonal mixed layer salinity balance of the tropical North Atlantic Ocean, *J. Geophys. Res., 113*(C2).

Fuenzalida, R., W. Schneider, J. Garcés-Vargas, L. Bravo, and C. Lange (2009), Vertical and horizontal extension of the oxygen minimum zone in the eastern South Pacific Ocean. *Deep Sea Research Part II: Topical Studies in Oceanography, 56*(16), 992-1003.

Garrett, C., and E. Kunze (2007), Internal tide generation in the deep ocean, *Annu. Rev. Fluid Mech., 39*, 57-87.

Geruo, A., J. Wahr, and S. Zhong (2012), Computations of the viscoelastic response of a 3-D compressible Earth to surface loading: an application to Glacial Isostatic Adjustment in Antarctica and Canada, *Geophys. J. Int., 192*, 557-572.

Gordon, A. L., C. F. Giulivi, J. Busecke, and F. M. Bingham (2015), Differences among subtropical surface salinity patterns. *Oceanography, 28*(1), 32-39.

Gould, W. J. (1985), Physical oceanography of the Azores Front. *Progress in Oceanography, 14*, 167-190.

Gu, G., R. F. Adler, G. J. Huffman, and S. Curtis (2007), Tropical rainfall variability on interannual-to-interdecadal and longer time scales derived from the GPCP monthly product. *J. Clim., 20*(15), 4033-4046.

Güntner, A., J. Stuck, S. Werth, P. Doll, K. Verzano, and B. Merz (2007), Aglobal analysis of temporal and spatial variations in continental water storage, *Water Resour. Res., 43*, W05416.

Haak, H., J. Jungclaus, U. Mikolajewicz, and M. Latif (2003), Formation and propagation of great salinity anomalies, *Geophys. Res. Lett., 30*(9).

Han, S. C., C. K. Shum, M. Bevis, C. Ji, and C. Y. Kuo (2006), Crustal dilatation observed by GRACE after the 2004 Sumatra-Andaman earthquake, *Science, 313*(5787), 658-662.

Held, I. M., and B. J. Soden (2006), Robust responses of the hydrological cycle to global warming, *J. Clim.*, *19*(21), 5686-5699.

Helm, K. P., N. Bindoff, and J. Church (2010), Changes in the global hydrological-cycle inferred from ocean salinity, *Geophys. Res. Lett., 37*, L18701.

Hosoda, S., T. Suga, N. Shikama, and K. Mizuno (2009), Global surface layer salinity change detected by Argo and its implication for hydrological cycle intensification, *J. Oceanography, 65,* 579-586.

Huntington, T. G. (2006), Evidence for intensification of the global water cycle: review and synthesis, J. Hydrology, 319(1), 83-95.

Johnson, G. C., and M. J. McPhaden (1999), Interior Pycnocline Flow from the Subtropical to the Equatorial Pacific Ocean. *J. Phys. Oceanography*, *29*(12), 3073-3089.

Köhl, A. (2015), Evaluation of the GECCO2 ocean synthesis: transports of volume, heat and freshwater in the Atlantic, *Q. J. R. Meteorol. Soc., 141*, 166-181.

Kusche, J., B. Uebbing, R. Rietbroek, C. K. Shum, and Z. H. Khan (2016), Sea level budget in the Bay of Bengal (2002-2014) from GRACE and altimetry, *J. Geophys. Res. Oceans, 121*, 1194-1217.

Labat, D. (2007), Wavelet analysis of the annual discharge records of the world's largest rivers, *Adv. Water Resour., 31*, 1.

Lagerloef, G., H. Y. Kao, O. Melnichenko, P. Hacker, E. Hackert, and Y. Chao (2013), Aquarius salinity validation analysis, *Aquarius Proj. Doc., AQ-014-PS-0016*, 36.

Lagerloef, G., R. Schmitt, J. Schanze, and H. Y. Kao (2010), The ocean and the global water cycle, *Oceanography, 23(4),* 82-93.

Lean, J. L., and D. H. Rind (2009). How will Earth's surface temperature change in future decades?, *Geophys. Res. Lett.*, *36(15),* L15708.

Llovel, W., S. Guinehut, and A. Cazenave (2010), Regional and interannual variability in sea level over 2002-2009 based on satellite altimetry, Argo float data and GRACE ocean mass, *Ocean Dyamics, 60*(5), 1193-1204.

Lukas, R. (2001), Freshening of the upper thermocline in the North Pacific subtropical gyre associated with decadal changes of rainfall. *Geophys. Res. Lett.*, *28*(18), 3485-3488.

McClain, C. R., S. R. Signorini, and J. R. Christian (2004), Subtropical gyre variability observed by ocean-color satellites, *Deep Sea Res. Part II: Topical Studies in Oceanography, 51*(1), 281-301.

McDougall, T. J., and P. M. Barker (2011), Getting started with TEOS-10 and the Gibbs Seawater (GSW) Oceanographic Toolbox, 28pp., SCOR/IAPSO WG127.

Melzer, B. A., & B. Subrahmanyam (2015), Investigating decadal changes in sea surface salinity in oceanic subtropical gyres, *Geophys. Res. Lett., 42*.

Metzger, E. J., O. M. Smedstad, P. G. Thoppil, H. E. Hurlburt, J. A. Cummings, A. J. Wallcraft, L. Zamudio, D. S. Franklin, P. G. Posey, M. W. Phelps, P. J. Hogan, F. L. Bub, and C. J. DeHaan (2014), US Navy operational global ocean and Arctic ice prediction systems. *Oceanography*, *27*(3), 32-43.

Monterey, G., and S. Levitus (1997), Seasonal Variability of Mixed Layer Depth for the World Ocean, *NOAA Atlas NESDIS 14*, 100, Natl. Oceanic and Atmos. Admin., Silver Spring, Md.

O'Connor, B. M., R. A. Fine, and D. B. Olson (2005), A global comparison of subtropical underwater formation rates, *Deep Sea Research Part I: Oceanographic Research Papers, 52*(9), 1569-1590.

Overland, J. E., S. Salo, and , J. M. Adams (1999), Salinity signature of the Pacific decadal oscillation, *Geophys. Res. Lett., 26*(9), 1337-1340.

Piecuch, C. G., and R. M. Ponte (2011), Mechanisms of interannual steric sea level variability, *Geophys. Res. Lett., 38*(15).

Qiu, B., and S. Chen (2005), Variability of the Kuroshio Extension Jet, Recirculation Gyre, and Mesoscale Eddies on Decadal Time Scales, *J. Phys. Oceanography, 35*, 2090-2103.

Qu, T., S. Gao, and I. Fukumori (2011), What governs the North Atlantic salinity maximum in a global GCM? *Geophys. Res. Lett., 38*(7).

Ramillien, A.C., and O. Brunau (2004), Global time variations of hydrological signals from GRACE satellite gravimetry, *Geophys. J. Int., 158*, 813-826.

Ramillien, G., A. Lombard, A. Cazenave, E. R. Ivins, M. Llubes, F. Remy, and R. Biancale (2006), Interannual variations of the mass balance of the Antarctica and Greenland ice sheets from GRACE, *Global and Planetary Change, 53*(3), 198-208.

Ren, L., E. Hackert, P. Arkin, and A. J. Busalacchi (2014), Estimating the global oceanic net freshwater flux from Argo and comparing it with satellite-based freshwater flux products, *J. Geophys. Res. Oceans, 119*(11), 7869-7881.

Reul, N., S. Fournier, J. Boutin, … S. Delwart (2013), Sea Surface Salinity Observations from Space with the SMOS Satellite: A New Means to Monitor the Marine Branch of the Water Cycle, *Surv. Geophys., 35*(3), 681-722.

Riser, S. C., L. Ren, and A. Wong (2008), Salinity in ARGO, *Oceanography, 21*(1), 56.

Riva, R. E. M., et al. (2009), Glacial Isostatic Adjustment over Antarctica from combined ICESat and GRACE satellite data, *Earth and Planetary Science Letters, 288*, 516-523.

Rodell, M., J. S. Famiglietti, J. Chen, S. I. Seneviratne, P. Viterbo, S. Holl ... and C. R. Wilson (2004), Basin scale estimates of evapotranspiration using GRACE and other observations, *Geophys. Res. Lett., 31*(20).

Romanovsky, V. E., D. S. Drozdov, N. G. Oberman, G. V. Malkova, A. L. Kholodov, S. S. Marchenko, … and D. A. Gilichinsky (2010), Thermal state of permafrost in Russia, *Permafrost and Periglacial Processes, 21*(2), 136-155.

Rosón, G., A. F. Rìos, F. F. Pèrez, A. Lavìn, and H. L. Bryden (2003), Carbon distribution, fluxes, and budgets in the subtropical North Atlantic Ocean (24.5°N), *J. Geophys. Res., 108*(C5).

Rudnick, D. L. (1996), Intensive surveys of the Azores Front: 2. Inferring the geostrophic and vertical velocity fields, *J. Geophys. Res.: Oceans*, *101*(C7), 16291-16303.

Sakumura, C., S. Bettadpur, and S. Bruinsma (2014), Ensemble prediction and intercomparison analysis of GRACE time-variable gravity field models, *Geophys. Res. Lett.*, *41*(5), 1389–1397.

Schmidt, R., S. Petrovic, A. Güntner, F. Barthelmes, J. Wünsch, and J. Kusche (2008), Periodic components of water storage changes from GRACE and global hydrology models, *J. Geophys. Res., 113*, B08419.

Schmitt, R. W. (2008), Salinity and the Global Water Cycle, *Oceanography, 21*(1), 12.

Skliris, N., R. Marsh, S. A. Josey, S. A. Good, C. Liu, and R. P. Allan (2014), Salinity changes in the World Ocean since 1950 in relation to changing surface freshwater fluxes, *Clim. Dyn., 43*,709-736.

Snyder, M. A., L. C. Sloan, N. S. Diffenbaugh, and J. L. Bell (2003), Future climate change and upwelling in the California Current, *Geophys. Res. Lett., 30*(15).

Stramma, L. (1992), The South Indian Ocean Current, *J. Phys. Oceanography, 22*(4), 421-430.

Swenson, S., and J. Wahr (2002), Estimated effects of the vertical structure of atmospheric mass on the time-variable geoid, *J. Geophys. Res., 107*(B9).

Tang, W., S. H. Yueh, A. G. Fore, and A. Hayashi (2014), Validation of Aquarius sea surface salinity with in situ measurements from Argo floats and moored buoys, *J. Geophys. Res. Oceans*, *119,* 6171–6189.

Taylor, K. (2001), Summarizing multiple aspects of model performance in a single diagram, *J. Geophys. Res., 106*(D7), 7183–7192, *J. Geophys. Res.-Atmospheres*, V106, D7.

Terray, L., L. Corre, S. Cravatte, T. Delcroix, G. Reverdin, and A. Ribes (2012), Near-surface salinity as nature's rain gauge to detect human influence on the tropical water cycle, *J. Clim.*, *25*(3), 958-977.

Timmerman, A., and H Goosse (2004), Is the wind stress forcing essential for the meridional overturning circulation, *Geophys. Res. Lett., 31*.

Trenberth, K. E. (2011), Changes in precipitation with climate change, *Clim. Res., 47,* 123.

Tychensky, A., P. Y. Le Traon, F. Hernandez, and D. Jourdan (1998), Large structures and temporal change in the Azores Front during the SEMAPHORE experiment. *J. Geophys. Res.: Oceans, 103*(C11), 25009-25027.

van den Broeke, M., et al. (2009), Partitioning recent Greenland mass loss, *Science, 326*, 984-986.

Vargas, G., S. Pantoja, J. A. Rutllant, C. B. Lange, and L. Ortlieb (2007), Enhancement of coastal upwelling and interdecadal ENSO-like variability in the Peru-Chile Current since late 19th century, *Geophys. Res. Lett.*, *34*(13).

Vega, A., Y. du-Penhoat, B. Dewitte, and O. Pizarro (2003), Equatorial forcing of interannual Rossby waves in the eastern South Pacific. *Geophys. Res. Lett.*, *30*(5).

Velicogna, I. (2009), Increasing rates of ice mass loss from the Greenland and Antarctic ice sheets revealed by GRACE, *Geophys. Res. Lett., 36*(19).

Vinogradova, N. T., and R. M. Ponte (2013a), Clarifying the link between surface salinity and freshwater fluxes on monthly to interannual time scales, *J. Geophys. Res.: Oceans, 118*(6), 3190-3201.

Vinogradova, N. T., and R. M. Ponte (2013b), Small-scale variability in sea surface salinity and implications for satellite-derived measurements, *J. Atmos. Oceanic Tech.*, *30*(11), 2689-2694.

Watkins, M. M., D. N. Wiese, D.-N. Yuan, C. Boening, and F. W. Landerer (2015), Improved methods for observing Earth's time variable mass distribution with GRACE using spherical cap mascons, *J. Geophys. Res. Solid Earth, 120*.

Wiese, D. N. (2015). GRACE monthly global water mass grids NETCDF RELEASE 5.0. Ver. 5.0. PO.DAAC, CA, USA. Dataset accessed [2016-05-23] at http://dx.doi.org/10.5067/TEMSC-OCL05.

Willis, J. K., D. P. Chambers, and R. S. Nerem (2008), Assessing the globally averaged sea level budget on seasonal to interannual timescales, *J. Geophys. Res., 113*, C06015.

Winton, M., & Sarachik, E. S. (1993), Thermohaline oscillations induced by strong steady salinity forcing of ocean general circulation models. *J. Phys. Oceanography*, *23*(7), 1389-1410.

Wu, L., W. Cai, L. Zhang, H. Nakamura, A. Timmermann, T. Joyce, ... and P. Chang (2012), Enhanced warming over the global subtropical western boundary currents, *Nature Climate Change, 2*(3), 161-166.

Yu, L. (2007), Global variations in oceanic evaporation (1958-2005): The role of the changing wind speed, *J. Clim., 20*(21), 5376-5390.

Yu, L. (2011), A global relationship between the ocean water cycle and near-surface salinity, *J. Geophys. Res., 116*, C10025.

Zhang, D., M.J. McPhaden, and W. E. Johns (2003). Observational Evidence for Flow between the Subtropical and Tropical Atlantic: The Atlantic Subtropical Cells. *J. Phys. Oceanography*, *33*(8), 1783-1797.

APPENDIX A

COPYRIGHT PERMISSIONS

A.1. CHAPTER 2 COPYRIGHT PERMISSIONS

Bryce Melzer <bmelzer@geol.sc.edu>
DTegbaru@agu.org
Subrahmanyam Bulusu <sbulusu@geol.sc.edu>,
Bryce Melzer <bmelzer@geol.sc.edu>
Thu, Oct 1, 2015 at 12:38 PM
GRL Permissions

Dear Mr. Tegbaru,

I am a graduate student at the University of South Carolina. I have published below GRL paper in recent issue and I will be using in my M.S Thesis as one of my chapters. I am the lead author on this paper. I need a letter of permission to use in my MS thesis. Below is full reference of the paper.

Melzer, B. A., and B. Subrahmanyam (2015), Investigating decadal changes in sea surface salinity in oceanic subtropical gyres, Geophys. Res. Lett., 42, doi:10.1002/2015GL065636.

Could you please send the letter by e-mail. Thank you.

Sincerely,
Bryce Melzer

Dawit Tegbaru <DTegbaru@agu.org>
Bryce Melzer <bmelzer@geol.sc.edu>
Subrahmanyam Bulusu <sbulusu@geol.sc.edu>,
grlonline <grlonline@agu.org>
Thu, Oct 1, 2015 at 1:26 PM
RE: GRL Permissions

Dear Bryce,

Thank you for writing. You may proceed with including your GRL article as part of your thesis. AGU's policy is that for non-commercial purposes, permission is required for reuse as long as proper attribution is given as follows:

"An edited version of this paper was published by AGU. Copyright (2015) American Geophysical Union."

It is recommended that the full citation and a link to the your article also be provided.

For more information visit: http://publications.agu.org/author-resource-center/usage-permissions/#repository.

Please let me know if there is anything I can do to further assist.

Dawit Tegbaru
Journal Program Manager
American Geophysical Union
+1.202.777.7418
DTegbaru@agu.org
www.agu.org